Identification and Regulation of a Hepatic Lipogenic Metabolon

Xiaotong Zhu[1, 2, 6], William B. McKean[3, 4], Tam Tran[1, 5], Xiaorong Fu[1, 2], Jay D. Horton[1, 2, 3, 7], Chai-Wan Kim[1, 2, 6]

1 Center for Human Nutrition, University of Texas Southwestern Medical Center, Dallas, TX 75390-9046

2 Department of Internal Medicine, University of Texas Southwestern Medical Center, Dallas, TX 75390-9046

3 Department of Molecular Genetics, University of Texas Southwestern Medical Center, Dallas, TX 75390-9046

4 START Center for Cancer Research, Mountain Region, West Valley City, UT 84119

5 Center of Excellence for Leukemia Studies, Department of Pathology, St. Jude Children's Research Hospital, Memphis, TN 38105

6 These authors contributed equally

7 Corresponding author

SUMMARY

De novo lipogenesis (DNL) plays a key role in the excessive fat accumulation present in Metabolic Dysfunction-Associated Steatotic Liver Disease (MASLD). Most mechanistic studies and experimental strategies for improving hepatic steatosis in MASLD have focused on the transcriptional regulation of enzymes involved in DNL and triglyceride (TG) synthesis. Here, we provide evidence for a post-translational mechanism that enhances fatty acid (FA) and TG synthesis through the assembly of a multi-protein lipogenic metabolon in liver. Under anabolic conditions, acetyl-CoA carboxylase 1 (ACC1) interacts with additional key enzymes in the DNL and TG synthesis pathway. Immunofluorescence and electron microscopy reveal that this lipogenic metabolon localizes around lipid droplets (LDs) and in proximity to mitochondria and LD interfaces in the anabolic state. The formation of the lipogenic metabolon facilitates the efficient transfer of FA synthesis intermediates to enhance lipogenic flux. These findings uncover a new nutrient-responsive, post-translational regulatory mechanism for hepatic lipogenesis and highlight the lipogenic metabolon as a potential therapeutic target for metabolic liver diseases.

Keywords

Liver metabolism, Metabolic Dysfunction-Associated Steatotic Liver Disease (MASLD), lipogenic metabolon, *de novo* lipogenesis, fatty acid synthesis, triglyceride synthesis, ACC1, metabolic diseases, post-translational regulation

INTRODUCTION

De novo lipogenesis (DNL) is the process in which fatty acids (FAs) are synthesized in cells from acetyl-CoA, primarily derived from carbohydrate metabolism [1]. Key transcriptional regulators of DNL, including SREBP-1c and ChREBP, are tightly regulated by hormones such as insulin [2,3] and glucagon [2], and through post-translational modifications of the DNL enzymes including phosphorylation [2] and acetylation [4,5]. In a healthy liver, DNL contributes to less than 5% of total hepatic triglycerides (TGs) [6-8]. However, in Metabolic Dysfunction-Associated Steatotic Liver Disease (MASLD), this contribution rises to 25-30% [9-11], due to insulin resistance, which leads to an increase in hepatic FA and TG synthesis [2,12-14]. Excessive TG accumulation in liver is associated with progression to metabolic-associated steatohepatitis (MASH), cirrhosis, and hepatocellular carcinoma [15-17]. With over one-third of U.S. adults affected by MASLD [18], it is crucial to elucidate the mechanisms driving aberrant hepatic FA synthesis in insulin-resistant states to identify potential therapeutic targets for FA-driven metabolic disorders.

Our previous studies have shown that the excessive activation of SREBP-1c initiates the transcription of genes encoding the enzymes necessary for FA synthesis, as well as the enzyme catalyzing the first step in glycerolipid synthesis [12,13]. This transcriptional program is a major driver of elevated FA and TG synthesis in insulin-resistant states [2,12,13], subsequently leading to hepatic steatosis, increased VLDL secretion, and hypertriglyceridemia [13,19-24]. The requirement of SREBP activation for the development of hepatic steatosis and hypertriglyceridemia was demonstrated by studies in which SCAP, a protein required for SREBP activation, was deleted in obese, insulin resistant mice (*ob/ob* mice) that normally have very high levels of hepatic FA and TG synthesis. SCAP deletion completely normalized rates of FA synthesis, liver TGs, VLDL secretion, and plasma TG levels [24] in *ob/ob* mice and hamsters. These results demonstrate that enhanced DNL is a major driver of steatosis in insulin-resistant livers.

FA and TG synthesis requires sequential enzymatic reactions distributed across multiple subcellular compartments. ATP citrate lyase (ACL) produces acetyl-CoA from citrate, acetyl-CoA synthetase 2 (ACSS2) synthesizes acetyl-CoA from acetate, acetyl-CoA carboxylases (ACC) 1 and 2 convert acetyl-CoA to malonyl-CoA, and fatty acid synthase (FAS) uses malonyl-CoA and

62 acetyl-CoA to generate palmitate (C16:0). These enzymes (except for ACC2 that is predominantly
63 localized to the outer mitochondrial membrane) are predominantly localized in the cytosol [25].
64 Palmitate can then be further desaturated by stearoyl-CoA desaturase (SCD1) or elongated by
65 ELOVL fatty acid elongase 6 (ELOVL6) before further desaturation, but unlike the enzymes
66 involved in the synthesis of palmitate, these proteins reside in the endoplasmic reticulum (ER)
67 [26,27]. Additionally, the first enzyme in glycerolipid synthesis, glycerol-3-phosphate acyltransferase
68 1 (GPAM), which acylates glycerol-3-phosphate to initiate TG and phospholipid synthesis is
69 located in the mitochondria [28]. How the FA and glycerolipid synthesis intermediates are efficiently
70 transferred among these spatially distributed enzymes to sustain continuous and efficient lipid
71 synthesis remains unclear.

72 One conceptual framework that could address this challenge is the metabolon hypothesis. In
73 1970, A.M. Kuzin first introduced the concept of physical enzyme–enzyme complexes. This idea
74 gained momentum in 1972 when P.A. Srere applied it to enzymes of the citric acid cycle,
75 highlighting their potential functional interactions [29]. Srere further expanded on this idea by coining
76 the term "metabolon" during a 1985 lecture in Debrecen, Hungary. He defined it as "a
77 supramolecular complex of sequential metabolic enzymes and cellular structural elements" [30],
78 emphasizing the functional coordination within cellular metabolic pathways. This concept has
79 been applied to explain the spatial organization of metabolic pathways such as the citric acid cycle
80 [31,32] and glycolysis [33], prompting us to examine whether hepatic FA and TG synthesis might also
81 be coordinated through spatial organization of lipogenic enzymes.

82 Here, we show that under anabolic conditions—such as high-carbohydrate feeding and insulin
83 resistance—FA and TG synthesis enzymes assemble into a functional lipogenic metabolon. This
84 complex enhances lipogenic flux by coordinating the sequential enzymatic reactions required to
85 synthesize the end product. This metabolon, including accessory proteins MIG12 and SPOT14
86 (S14) [34], predominantly localizes around lipid droplets (LDs) in primary hepatocytes. Together,
87 these findings reveal a dynamic multi-enzyme complex that facilitates FA and TG synthesis and
88 provides new insights into the spatial organization and coordinated regulation of hepatic lipid
89 synthesis.

90 RESULTS

91 Identification of the lipogenic complex in liver

92 The first indication that a lipogenic complex might exist grew out of investigations focused on
93 determining the function of a poorly characterized protein, S14. S14 is highly expressed in

94 lipogenic tissues [35], and its gene transcription is regulated by SREBP-1c [36,37], carbohydrate-
95 responsive element-binding protein (ChREBP) [38], and thyroid hormone receptor (TR) [39], which
96 suggests that it may play a role in lipogenesis. Deletion of S14 in mice reduced lipid synthesis in
97 liver [34] and lactating mammary glands [40], although its exact function in lipogenesis has not been
98 elucidated. To further define the function of S14, we used an adenovirus that expressed S14 with
99 a Flag tag in mice and carried out immunoprecipitation of S14 from liver lysates to identify potential
100 interacting proteins. LC/MS analysis revealed that MIG12, ACC1, FAS, and β-tubulin all co-
101 immunoprecipitated with S14 (Figure 1A). MIG12, a protein we previously showed that promotes
102 the polymerization of ACC1 and ACC2 [41], shares 32% sequence identity with S14 [41] and can
103 form a heterodimer with S14 [34]. To further confirm that the association of these enzymes co-
104 immunoprecipitated with S14 reflects physical interaction in cells, we performed
105 immunofluorescence staining in primary hepatocytes isolated from rats refed a fat-free, high-
106 carbohydrate diet (FFD). ACC1, MIG12, and S14 prominently co-localized around LD–associated
107 ER regions. Quantitative analysis using Pearson's correlation (above Costes threshold)
108 demonstrated strong spatial overlap among the three enzyme pairs, with ACC1–S14 (R = 0.73),
109 ACC1–MIG12 (R = 0.52), and S14–MIG12 (R = 0.52) (Supplemental Table 1). These data
110 indicate that ACC1, S14, and MIG12 occupy shared subcellular domains under conditions of high
111 lipogenesis, supporting the existence of a coordinated lipogenic enzyme complex in hepatocytes
112 (Figure 1B). Representative ROIs and pixel-intensity histograms are shown in Figure S1, and
113 detailed colocalization metrics, including Manders' coefficients and Costes statistics, are provided
114 in Supplemental Table 1.

115 Co-localization of proteins involved in lipogenesis around LDs in hepatocytes

116 To investigate potential additional interactions among lipogenic proteins, we used antibodies
117 recognizing various lipogenic enzymes in primary hepatocytes to assess co-localization by
118 confocal immunofluorescence. As shown in Figure 1, co-localization was quantified using
119 Pearson's correlation coefficient (Pearson's R) in LD-enriched regions where the enzyme signals
120 were concentrated. Immunofluorescence imaging of primary hepatocytes isolated from rat livers
121 refed a FFD demonstrated that ACC1 co-localized with ACL (R ≈ 0.83), ACSS2 (R ≈ 0.46), and
122 FAS (R ≈ 0.55) around LDs, despite their known localization in the cytosol. GPAM, a mitochondrial
123 outer membrane protein involved in glycerolipid synthesis, also co-localized with ACC1 in LD-
124 associated regions (R ≈ 0.51). In contrast, the gluconeogenic enzyme PEPCK, which is unrelated
125 to lipogenesis, showed almost no overlap with ACC1 (R ≈ 0.11), likely because it remains confined
126 to the cytosol and does not redistribute to LD-proximal regions (Figure 2A, Supplemental Table

127 2). Comprehensive testing metrics, including Manders' coefficients and Costes significance
128 testing, are provided in Supplemental Table 2 and further support the robust spatial association
129 of ACC1 with multiple cytosolic lipogenic enzymes, whereas the non-lipogenic negative control,
130 PEPCK, showed only minimal overlap with ACC1. Adipose differentiation-related protein (ADRP),
131 an LD-resident protein, marked LDs where ACL, ACC1, and FAS also localized in primary
132 hepatocytes from refed rats (Figure 2B). Three-dimensional imaging further confirmed the
133 localization of ACC1 surrounding LDs in primary hepatocytes from refed rats (Figure 2C).
134 Additional imaging across various fasting and refeeding timepoints suggested that ACC1-
135 containing complexes assemble progressively during metabolic activation and accumulate
136 around LDs in rat primary hepatocytes (Figure S2).

137 Co-localization of proteins involved in lipogenesis at the interface of mitochondria 138 and LDs in hepatocytes

139 Electron microscopy (EM) with immunogold labeling using antibodies recognizing ACC1 or FAS
140 was used to determine their subcellular localization in primary hepatocytes from refed rats.
141 Consistent with the immunofluorescence images (Figure 2C; Figure S2), EM revealed that ACC1
142 localized predominantly around LDs (Figure 3A). This finding was further supported by
143 immunofluorescence imaging and EM performed on the same hepatocyte (Figure S3A). Double
144 immunogold labeling using different sizes of gold particles for ACC1 and FAS demonstrated their
145 co-localization around LDs (Figure 3B; Figure S3B–C). Although ACC1 and FAS were
146 occasionally observed near the ER, they were much more consistently enriched around LDs
147 (Figure S3D). This pattern aligned with staining of the ER marker protein disulfide isomerase
148 (PDI), which showed only limited overlap with ACC1, in contrast to the strong co-localization
149 observed between ACC1 and LDs (Figure S3E).

150 Notably, interactions between ACC1 and FAS were also observed at interfaces between
151 mitochondria and LDs (Figure 3C). Subcellular fractionation of liver lysates from FFD-refed rats
152 further demonstrated that ACL, ACC1, ACC2, FAS, SCD1, and GPAM were present in both LD
153 and mitochondrial fractions, regardless of their canonical localizations in the cytoplasm,
154 mitochondria, or ER (Figure 3D). EM frequently revealed mitochondria positioned adjacent to
155 LDs (Figure S3F), and GPAM localization was subsequently confirmed to be on the outer
156 mitochondrial membrane, including sites where mitochondria interface with LDs (Figure S3G).
157 Subcellular fractionation of liver lysates from FFD-refed rats further confirmed this finding,
158 whereas mitochondrial inner membrane proteins, such as prohibitin and cytochrome c, were
159 found only in the mitochondrial fraction (Figure S3H).

160 Combined, these findings demonstrate that lipogenic proteins co-localize around LDs and at
161 mitochondria–LD contact sites under high lipogenesis conditions.

162 Active dephosphorylated ACC promotes polymerization, enhances lipogenesis, 163 and increases LD localization

164 ACC activity is acutely regulated through phosphorylation and dephosphorylation. AMP-activated
165 protein kinase (AMPK) phosphorylates ACC at Ser-79 [42,43], inhibiting its enzymatic activity through
166 largely undefined mechanisms [44,45]. Fasting or glucagon treatment increases AMPK activity,
167 whereas insulin suppresses AMPK activity and stimulates the Mg^{2+}-dependent protein
168 phosphatase 2A (PP2A), which dephosphorylates ACC, thereby increasing its activity [46-50]. During
169 refeeding, ACC is converted from its phosphorylated inactive form to its dephosphorylated, active
170 form due to stimulation of protein phosphatase activity. This dephosphorylation activates ACC
171 and DNL in hepatocytes, allowing excess glucose to be converted into FAs and TGs for storage
172 [51,52].

173 We next determined whether the phosphorylated state of ACC affected the formation of the
174 lipogenic complex. For this study, we treated rat primary hepatocytes with 5-aminoimidazole-4-
175 carboxamide ribonucleoside (AICAR), an AMPK agonist, to induce ACC phosphorylation [53]. The
176 primary hepatocytes were incubated with 1 mM AICAR and cell lysates were prepared at 0, 1.5,
177 and 3 hours after treatment. SDS-PAGE immunoblot analysis of cell lysates showed an increase
178 in phosphorylated ACC levels in the AICAR-treated cells compared to the untreated cells;
179 however, the amount of total ACC protein was unchanged (Figure 4A). Blue native PAGE analysis
180 of cell lysates demonstrated that the polymerized, higher molecular weight form of ACC1 was
181 present only in untreated primary hepatocytes and was disrupted in AICAR-treated hepatocytes
182 (Figure 4A). Even with MIG12 overexpression, which robustly promotes ACC1 polymerization,
183 AICAR reduced the higher molecular weight form of ACC1 to baseline (Figure 4B). Consistent
184 with reduced polymerization, FA synthesis measured by ^{3}H-acetate incorporation into newly
185 synthesized FAs fell ~6-fold within 30 minutes of AICAR treatment (Figure 4C), while FA-synthesis
186 enzyme levels remained unchanged (Figure S4A). Collectively, these results imply that the rapid
187 decrease in DNL results from AMPK-mediated ACC phosphorylation, which disrupts ACC1
188 polymerization.

189 To further explore the role of dephosphorylated ACC in promoting DNL *in vitro*, we blocked
190 endogenous phosphatase activity in liver cytosol using a phosphatase inhibitor cocktail (Figure
191 4D). Immunoblot analysis confirmed that the inhibitor prevented ACC dephosphorylation,

192 whereas λ-phosphatase enhanced dephosphorylation (Figure S4B). Compared with the inhibitor-
193 treated group, untreated liver cytosol, which underwent dephosphorylation during incubation,
194 showed a 4-fold increase in palmitate synthesis rates in a citrate concentration-dependent manner
195 (Figure 4D). Furthermore, in primary hepatocytes from refed rats, ACC1 localized around LDs
196 under DMSO control, consistent with Figures 1–3, but this LD-associated pattern was significantly
197 reduced with AICAR treatment (Figure 4E).

198 Taken together, these findings demonstrate that the polymerization of ACC, mediated by
199 dephosphorylation, is critical for its localization with other lipogenic enzymes around LDs and for
200 regulating DNL in hepatocytes.

201 The interaction of ACC1 with lipid synthesis-associated proteins is enhanced when 202 ACC is in the activated state

203 As demonstrated above, ACC1 polymerizes and co-localizes with other lipogenic proteins around
204 LDs under high DNL conditions. To determine how ACC1 interactions with other proteins change
205 upon activation, we performed ACC1 immunoprecipitation from mouse liver lysates incubated
206 with 5 mM $MgCl_2$ at 30°C for 30 minutes with or without a phosphatase inhibitor cocktail. With
207 endogenous phosphatases active, ACC1 co-immunoprecipitated ACC2, ACSS2, FAS, ACL,
208 GPAM, MIG12, S14, and SCD1 (Figure 5A). Notably, β-actin, a cytoskeletal protein, also showed
209 significant binding to ACC1, suggesting that cytoskeletal components might play a role in the
210 formation of the lipogenic complex. In contrast, these interactions were markedly reduced when
211 endogenous phosphatases were inhibited, suggesting that ACC1 interacts more strongly with
212 other proteins in a phosphatase-active state. Proteins unrelated to lipid synthesis, such as
213 PEPCK, prohibitin, cytochrome c, and PDI, did not bind ACC1 under either condition.

214 Notably, ACC2 maintained strong binding to ACC1 even in the presence of phosphatase
215 inhibitors, suggesting that ACC1 and ACC2 form a relatively stable heteromer. These
216 observations are supported by immunoprecipitation of liver lysates from hepatocyte-specific
217 ACC1 or ACC2 knockout mice, which revealed a clear reciprocal interaction between the two
218 enzymes (Figure S5A). Blue native PAGE analysis further supported this model: whereas ACC1
219 migrated similarly in wild-type and ACC2-deficient livers, ACC2 showed a markedly altered
220 pattern in ACC1-deficient livers. In normal liver, ACC2 predominantly appeared as a dimer or
221 tetramer, but in the absence of ACC1, ACC2 shifted toward higher–molecular-weight, more
222 polymerized species (Figure S5B). Considering that hepatic ACC2 expression is substantially

223 lower than ACC1, these findings suggest that, under physiological conditions, most endogenous
224 ACC2 may exist as a heterodimer with ACC1.

225 Immunofluorescence analysis in cultured cells provided additional evidence for the ACC1–ACC2
226 heterodimer. ACC1 was detected predominantly in the cytosol when expressed alone (Figure
227 S5C). However, when co-transfected with ACC2, a substantial fraction of ACC1 colocalized with
228 ACC2 at the mitochondria (Figure S5D). In addition to this mitochondrial pool, ACC1 also
229 displayed cytosolic localization that did not overlap with ACC2. These observations indicate that
230 ACC1 is present in the cytosol but also at the mitochondrial membrane as a complex with ACC2.

231 To determine whether endogenous ACC2 influences ACC1-mediated protein interactions, we
232 immunoprecipitated ACC1 from refed wild-type and ACC2 hepatocyte-specific knockout livers,
233 using ACC1-deficient mice as a negative control. Co-precipitation of ACL, ACSS2, FAS, S14,
234 SCD1, GPAM, β-actin, and β-tubulin was reduced to varying degrees in ACC2-deficient livers
235 compared with wild-type (Figure 5B), suggesting that ACC2 contributes to the stability or
236 assembly of ACC1-associated protein complexes. MIG12 binding to ACC1 was unaffected by
237 phosphatase inhibition (Figure 5A) or by the absence of ACC2 (Figure 5B), consistent with its
238 direct association with ACC1. As expected, PEPCK, prohibitin, cytochrome c, and calnexin were
239 not co-immunoprecipitated with ACC1 in any group.

240 Given that ACL, ACSS2, ACC, FAS, SCD1, and the mitochondrial GPAM participate in ACC1-
241 associated complexes, we next measured TG synthesis under phosphatase active versus
242 phosphatase-inactive conditions. Glycerol 3-phosphate (G3P) was used as a substrate with
243 excess oleoyl-CoA added to liver homogenates from refed rats to test whether TG synthesis via
244 GPAM is enhanced when endogenous phosphatases are active, a condition that favors lipogenic
245 complex formation (Figure S5E). The results demonstrated that TG synthesis was significantly
246 higher under phosphatase-active conditions and increased further with rising $MgCl_2$
247 concentrations, paralleling $MgCl_2$-dependent ACC1 dephosphorylation (Figure S4B), whereas
248 under phosphatase inactive conditions, TG synthesis remained unchanged with $MgCl_2$ (Figure
249 S5E).

250 These results demonstrate that phosphorylation–dephosphorylation regulates both FA and TG
251 synthesis in part by controlling ACC1-mediated lipogenic complex formation.

252 **Lipogenic metabolon formation facilitates FA synthesis**

253 To confirm the interactions between ACC1 and the other FA synthesis proteins, and to assess
254 the regulatory effects of phosphorylation and dephosphorylation on the activities of individual FA
255 synthesis enzymes *in vitro*, we conducted a comprehensive purification of recombinant ACSS2,
256 ACC1, FAS, MIG12, and S14 in mammalian cells using Ni-NTA resin and gel-filtration
257 chromatography (Figure 6A, S6A), and rPEPCK was purified as a negative control (Figure S6B).
258 The recombinant protein mixture was dephosphorylated with λ-phosphatase and
259 immunoprecipitation was performed with anti-ACC1 antibodies. Immunoblot analysis (Figure 6B)
260 revealed that all other recombinant FA synthesis proteins co-immunoprecipitated with rACC1,
261 whereas rPEPCK did not. These results confirm that recombinant ACC1 interacts with core
262 lipogenic factors *in vitro* using recombinant proteins (Figure 6B).

263 Next, we pre-incubated the individual recombinant proteins or their mixtures with λ-phosphatase
264 to simulate the DNL activated environment as described above. Parallel groups without λ-
265 phosphatase treatment were used as phosphorylated controls. Figure S6C shows that each
266 purified protein exhibited functional activity, and interestingly, all tested lipogenic proteins
267 displayed increased activity to varying degrees when dephosphorylated compared to their
268 phosphorylated forms. However, rACC1 exhibited the greatest increase in enzymatic activity upon
269 λ-phosphatase treatment compared with the other lipogenic enzymes. Next, we combined purified
270 lipogenic enzymes, rACL-rACC1-rFAS or rACSS2-rACC1-rFAS, and measured FA synthesis
271 from citrate or acetate, respectively. As predicted, rACL-rACC1-rFAS activity was nearly four
272 times higher with λ-phosphatase treatment compared with untreated conditions (Figure 6C).
273 Similarly, rACSS2-rACC1-rFAS activity increased by ~3.5-fold upon λ-phosphatase treatment
274 relative to untreated conditions (Figure 6C). Figure S6D shows the phosphorylation levels of
275 rACC1 alongside total rACC1 levels at various time points following λ-phosphatase treatment,
276 demonstrating that λ-phosphatase efficiently dephosphorylates proteins without altering their total
277 levels.

278 Inasmuch as each rACL, rACSS2, rACC1, and rFAS protein exhibited increased enzymatic
279 activity in the dephosphorylated state, these observations alone could not distinguish whether the
280 enhanced palmitate production resulted from cooperative complex formation or simply reflected
281 additive increases in the intrinsic activities of individual enzymes upon dephosphorylation. To
282 directly address this issue, we performed a FA-synthesis assay using (1) liver cytosol alone, (2)
283 recombinant ACL–ACC1–FAS alone, and (3) a mixture of liver cytosol and recombinant ACL–
284 ACC1–FAS, with protein amounts normalized across conditions. Each group was subjected to
285 either dephosphorylated or phosphorylated conditions under identical treatment settings. As

286 shown in Figure S6E, dephosphorylation was successfully achieved in all conditions. Under
287 dephosphorylated conditions, combining liver cytosol with recombinant ACL–ACC1–FAS
288 produced substantially greater palmitate than the expected additive activity calculated from
289 cytosol alone and recombinant enzymes assayed in parallel (Figure 6D). This enhancement
290 exceeded what would be predicted from simple additive effects of dephosphorylation on individual
291 enzymes and was supported by a significant interaction between phosphorylation state and
292 mixing condition (two-way ANOVA, $F(3,16) = 133.4$, $P < 0.0001$). Together, these data indicate
293 a strong synergistic increase in lipogenesis arising from cooperative interactions between
294 dephosphorylated cytosolic proteins and recombinant enzymes. In contrast, under
295 phosphorylated conditions, the palmitate produced by the combined reaction was
296 indistinguishable from the expected additive activity (Figure 6E), indicating that cooperative
297 assembly and synergistic flux enhancement are selectively enabled by dephosphorylation.

298 To directly assess complex formation under these conditions, ACC1 was immunoprecipitated
299 from the same reaction mixtures. Consistent with the results shown in Figure 5A,
300 dephosphorylation markedly enhanced the interactions of ACC1 with FAS and ACL, and β-tubulin
301 as determined by co-precipitation studies, suggesting that the lipogenic metabolon may be
302 functionally linked to cytoskeletal components (Figure S6F). No nonspecific binding was observed
303 with control rabbit IgG.

304 While it is not feasible to systematically test all cytosolic proteins that could potentially contribute
305 to metabolon assembly, Figure 5 identified structural proteins as representative non-lipogenic
306 factors that interact with ACC1 under dephosphorylated conditions. Consistent with this
307 observation, β-tubulin showed detectable co-localization with ACC1 around lipid droplets in
308 primary hepatocytes under lipogenic refeeding conditions (Pearson's $R \approx 0.32$), whereas this
309 spatial association was markedly reduced upon fasting (Figure 6F). In parallel, pharmacological
310 perturbation of microtubule dynamics provided support for the role of cytoskeleton in lipogenesis.
311 Disrupting microtubule polymerization with nocodazole consistently decreased FA synthesis in
312 primary hepatocytes, whereas stabilizing microtubules with taxol, an agent with the opposite effect
313 of nocodazole, had minimal impact on lipogenesis (Figure 6G). These observations suggest that
314 intact cytoskeletal architecture facilitates lipogenesis by coordinating the nutrient-responsive
315 assembly and spatial organization of lipogenic enzyme complexes, rather than directly regulating
316 microtubule dynamics.

317 Collectively, these findings suggest that lipogenic activity is enhanced through post-translational
318 regulation that promotes the formation of a functional lipogenic metabolon under physiological

319 conditions favoring high DNL. This process likely involves dynamic and cooperative interactions
320 among DNL- and TG-related enzymes, aided by structural proteins and other accessory factors,
321 allowing for more integrated and efficient lipogenesis.

322 ACC1 anchors a multi-module lipogenic network integrating translation, 323 trafficking, and lipid metabolism

324 To further map the ACC1-centered protein network, we immunoprecipitated ACC1 from wild-type
325 and ACC-deficient liver lysates. In parallel, MIG12 and S14, two direct ACC1-binding partners
326 were immunoprecipitated, as was ACSS2, a representative lipogenic enzyme, to compare their
327 interaction profiles (Figure 7A). MIG12 and S14 pulldowns closely mirrored the ACC1
328 immunoprecipitation pattern: proteins enriched in wild-type lysates were markedly reduced in
329 ACC-deficient lysates, consistent with their direct association with ACC1 and the dependence of
330 their interactomes on ACC1 integrity. In contrast, ACSS2 immunoprecipitation showed a distinct
331 profile. Although several lipogenic enzymes were reduced in ACC-deficient lysates, ACSS2
332 retained clear interactions with multiple lipogenic proteins. This pattern suggests that ACC1
333 enhances or stabilizes the overall lipogenic assembly rather than acting as its sole organizing
334 component. Notably, β-actin binding to ACSS2 was unchanged regardless of ACC1 status,
335 implying that actin contributes to complex organization through an ACC1-independent
336 mechanism.

337 We next quantified proteins co-immunoprecipitated with ACC1 by mass spectrometry. Proteins
338 that were reduced by >20-fold in ACC1, MIG12, or S14 immunoprecipitations from ACC-deficient
339 lysates were classified as ACC1-dependent interactors. STRING network analysis of these
340 proteins resolved three highly connected clusters (Figure 7B, top). The largest cluster consisted
341 of ribosomal and translation-associated proteins, suggesting that a robust interface between
342 ACC1 and the translational machinery exists. A second cluster was enriched for vesicle/trafficking
343 components and cytoskeletal protein-binding factors, indicating that ACC1 is embedded within a
344 broader transport and structural scaffold. A third cluster consisted of enzymes involved in FA
345 synthesis and remodeling, consistent with ACC1's canonical metabolic function (Figure 7B,
346 bottom). DAVID functional annotations performed on the same dataset produced closely matching
347 categories (Figure S7 and Supplemental Table 3).

348 Together, these findings indicate that activated ACC1 functions as a central organizational hub
349 that coordinates core lipogenic enzymes—including FAS, ACL, ACSS2, SCD1, GPAM, and
350 ACC2—into a coherent metabolic assembly. Direct binding by MIG12 and S14 likely stabilizes

351 this structure, while cytoskeletal and trafficking components associate with the ACC1-centered
352 complex to support spatial organization and substrate delivery. The presence of ribosomal
353 proteins and transport-associated factors among ACC1-dependent interactors further suggests
354 that lipogenesis is integrated with protein synthesis and intracellular trafficking through multiple
355 points of connection.

356 **DISCUSSION**

357 Transcriptional control of FA and TG synthesis is well characterized [54], but much less is known
358 about how lipid synthesis is regulated post-transcriptionally. Here, we identified a previously
359 unrecognized post-translational mechanism in which hepatic lipogenic enzymes assemble into a
360 multi-protein metabolon under anabolic conditions. This metabolon provides a spatial basis for
361 efficient glycerolipid synthesis and introduces a new dimension to the regulation of DNL.

362 Using immunofluorescence and EM, we showed that enzymes involved in FA and TG synthesis,
363 along with accessory proteins like MIG12 and S14, co-localize around LDs and function as an
364 integrated multi-enzyme assembly rather than as isolated enzymes under physiological activation
365 states such as high carbohydrate feeding. These findings build on earlier LD proteomics reports
366 that identified ACC1 [55-59] and FAS [58] on LDs, extending them by providing direct structural
367 visualization of their co-localization in mammalian hepatocytes. Furthermore, the proximity
368 between cytosolic enzymes such as ACC1 and FAS and the mitochondrial enzyme GPAM at
369 contact sites suggests coordinated substrate transfer into the glycerolipid pathway. Subcellular
370 fractionation of liver lysates from high-carbohydrate-refed rats further supports these
371 observations.

372 Immunoprecipitation of ACC1 from liver lysates incubated under phosphatase-active conditions
373 revealed robust interactions between ACC1 and multiple lipogenic proteins, whereas the inclusion
374 of phosphatase inhibitors markedly reduced these associations (Figure 5A). This biochemical shift
375 was paralleled by *in vitro* FA and TG synthesis assays, in which phosphatase-active conditions
376 produced substantially higher lipid synthesis than phosphatase-inhibited ones. We initially
377 attributed this enhanced interaction and activity to ACC1 dephosphorylation, a hypothesis
378 supported by *in vivo* experiments using the AMPK agonist AICAR. In primary hepatocytes isolated
379 from high-carbohydrate–refed rats, AICAR treatment caused the activated, polymerized form of
380 ACC1 to dissociate into its inactive dimeric form, as shown by blue native PAGE. The extensive
381 polymerization of ACC1 driven by MIG12 overexpression was also significantly reduced by
382 AICAR-mediated ACC1 phosphorylation. Correspondingly, short-term AICAR treatment

383 significantly suppressed hepatic lipogenesis in primary hepatocytes without affecting the steady-
384 state levels of lipogenic enzymes and markedly reduced ACC1 localization around LDs. Notably,
385 ACC1 was not the only enzyme influenced by dephosphorylation, as phosphatase treatment also
386 increased the enzymatic activities of rACSS2 and rFAS, although to a lesser extent than ACC1.
387 These findings suggest that anabolic phosphatase-active states coordinate multiple components
388 of the lipogenic pathway, collectively enhancing metabolon assembly and catalytic output.

389 Another notable finding from the immunoprecipitation experiments was the strong interaction of
390 ACC1 with ACC2 and MIG12. Whereas most ACC1-associated proteins showed enhanced
391 binding under phosphatase-active conditions, ACC2 and MIG12 maintained stable interactions
392 with ACC1 irrespective of its phosphorylation state. This feature suggests that these two proteins
393 form a relatively stable core structural interaction with ACC1.

394 Additional insight into ACC2 was obtained from transfection studies in CHO-K1 cells. When ACC1
395 and ACC2 were co-expressed, the fraction of ACC1 that interacted with ACC2 and formed
396 heterodimers or higher-order heteromultimers and localized to mitochondria increased (Figure
397 S5D). ACC1 also retained a substantial cytosolic pool that did not overlap with ACC2, likely
398 reflecting cytosolic homomeric ACC1 assemblies. These observations indicate that ACC1 is
399 partitioned between heteromeric ACC1–ACC2 complexes at mitochondria and homomeric ACC1
400 assemblies in the cytosol and suggest that the subcellular localization and functional partitioning
401 of malonyl-CoA–producing acetyl-CoA carboxylase activity may be influenced by the relative
402 abundance of ACC2. These findings are consistent with the tissue-specific expression patterns
403 of ACC isoforms. In liver and adipose tissue, where malonyl-CoA is used primarily for lipogenesis,
404 ACC1 is the predominant isoform; whereas in muscle and heart, where malonyl-CoA mainly
405 inhibits mitochondrial fatty acid oxidation, ACC2 is the major form. Thus, cells may regulate the
406 relative abundance (stoichiometry) of ACC1 and ACC2 to redistribute acetyl-CoA carboxylase
407 activity between the cytosol and mitochondria according to metabolic demands. In this context,
408 ACC1–ACC2 interactions may serve as a regulatory node linking FA synthesis and oxidation.
409 Alterations in the stoichiometry of the two isoforms could therefore shift the balance between
410 lipogenesis and control of mitochondrial FA oxidation by modulating the subcellular distribution of
411 carboxylase activity.

412 Finally, although ACC2 has long been viewed primarily as a regulator of mitochondrial FA
413 oxidation, ACC2 deletion reduced ACC1 interactions with multiple lipogenic enzymes and
414 structural proteins (Figure 5B). This finding supports the view that ACC2 functions not only as a
415 metabolic enzyme that inhibits FA oxidation but also as a structural component essential for the

416 organization and maintenance of the lipogenic metabolon. Complementing these structural
417 insights, our biochemical assays demonstrated that assembling lipogenic enzymes within a
418 shared reaction environment generates catalytic outputs that exceed the sum of individual
419 activities. Under DNL-activated conditions, combining recombinant ACL–ACC1–FAS with liver
420 cytosol nearly doubled the FA synthesis compared with the expected additive activity, indicating
421 synergistic enhancement of pathway flux. This synergy suggests that enzyme co-assembly, rather
422 than simply increased intrinsic activity, facilitates more efficient substrate channeling during active
423 lipogenesis. These functional observations reinforce the multi-module organization described in
424 Figure 7, in which ACC1 immunocomplexes interact not only with lipogenic enzymes but also with
425 ER-proximal translation components, vesicle-movement proteins, and actin-linked scaffolds,
426 supporting the concept that lipogenic enzymes achieve maximal efficiency when spatially
427 integrated with cytoskeletal scaffolds and intracellular transport machinery, and when functionally
428 linked to translation-associated components.

429 Although metabolon-based regulation is less explored in lipogenesis, analogous mechanisms
430 have been established in the TCA cycle and glycolysis [29-31,60-63]. The substrate-responsive
431 assembly of PFK filaments in the presence of fructose-6-phosphate [64] provides a relevant
432 precedent and parallels ACC1 filament formation under anabolic conditions, suggesting that these
433 filaments may serve as structural scaffolds for metabolon assembly. Consistent with this concept,
434 a FA–synthesis metabolon has been described in the thermophile *Chaetomium thermophilum* [65]
435 and ACC–FAS co-localization has been visualized in *Saccharomyces cerevisiae* [66], where these
436 enzymes are reorganized or sequestered in response to glucose starvation. These observations
437 across lower eukaryotes support the idea that nutrient state governs the assembly and
438 disassembly of spatially organized lipogenic enzymes.

439 Recent work by Wijesinghe *et al.* [67] extends this concept to mammalian cells. In their study, ACC1
440 formed ring-like puncta and localized to the surface of lipid droplets (LDs), but this localization
441 was highly conditional: anabolic cues such as AMPK inhibition preserved ACC1–LD co-
442 localization, whereas large LDs generated by acute oleic-acid loading—which diminishes
443 anabolic drive—displayed reduced ACC1 staining. This pattern mirrors our observation that the
444 AMPK agonist AICAR suppresses ACC1 accumulation around LDs (Figure 4E), indicating that
445 ACC1 recruitment to LDs requires appropriate metabolic activation rather than merely reflecting
446 LD abundance. Together, these findings align with our model in which ACC1 polymerization and
447 its interactions with accessory factors generate a nutrient-responsive lipogenic complex in
448 hepatocytes. Collectively, the emerging evidence across species supports a broader framework

449 in which ACC1 integrates nutrient status with spatial enzyme organization to optimize lipogenesis
450 during anabolic transitions.

451 In conclusion, our study demonstrates that under anabolic conditions, hepatic lipogenic enzymes
452 assemble into a spatially organized, phosphorylation-responsive metabolon around LDs. This
453 multi-protein metabolon enhances catalytic efficiency facilitating improved transfer of
454 intermediates between sequential enzymes, thereby supporting efficient synthesis of FA and TGs.
455 These findings provide a mechanistic foundation for understanding hepatic lipid synthesis and
456 highlight therapeutic opportunities in metabolic disease by targeting the structure and regulation
457 of the lipogenic metabolon.

458 Limitations of the study

459 In this study, we present evidence for a novel post-translational regulatory mechanism that
460 enhances FA and TG synthesis in the liver via the assembly of a multi-protein metabolon. Ideally,
461 since the structure of ACC1 under different activation states has been reported [68,69], we would
462 have included structural analyses of this ACC1 mediated lipogenic metabolon. However,
463 detecting such metabolons presents greater challenges compared to stable protein assemblies.
464 The reason is that a metabolon is characterized as a transient structural-functional metabolon
465 formed by sequential enzymes within a metabolic pathway, exhibiting non-covalent interactions
466 and associating with various cellular structural elements, such as integral membrane proteins and
467 cytoskeletal components [30,70]. Consequently, the interactions among these proteins are more
468 transient and dynamic, enabling them to adapt to fluctuations in metabolic environments.

469 Additionally, the mRNA levels of the lipogenic proteins are all significantly downregulated during
470 fasting as a result of reduced SREBP-1c expression, which restricted our ability to compare the
471 co-localization of lipogenic proteins between fasting and refeeding conditions. Therefore, we
472 employed AICAR treatment and elevated phosphorylation levels to simulate catabolic states *in*
473 *vivo* and *in vitro*, respectively.

474 Declaration of generative AI and AI-assisted technologies in the writing process

475 During the preparation of this manuscript, the authors used ChatGPT (OpenAI) solely for
476 language editing, including grammar correction and improvement of clarity. No content, data
477 interpretation, or scientific conclusions were generated by the tool. After using this assistance,
478 the authors thoroughly reviewed, revised, and approved all text, and they take full responsibility
479 for the integrity and accuracy of the final manuscript.

RESOURCE AVAILABILITY

Lead contact

Further information and requests for resources should be directed to the lead contact, Jay D. Horton (jay.horton@utsouthwestern.edu).

Materials availability

Custom antibodies generated in this study are available upon reasonable request and completion of an MTA. Cloning constructs are available from the Lead Contact. All other materials used in this study are specified in the key resources table.

Data and code availability

All data supporting the findings are available within the paper and Supplemental Information. No custom code was used.

ACKNOWLEDGEMENTS

We thank Norma Anderson, Judy Sanchez, Tuyet Dang, and Tessa Edwards for excellent technical assistance; Lisa Beaty for suspension cell culture and set up; Linda Donnelly for assistance with antibody generation; Jinhai Yu for providing TEV protease; and Chelsea Burroughs and Nancy Heard for help with graphics. The work was supported by grants NIH P01HL160487 and NIH P30DK127984.

AUTHOR CONTRIBUTIONS

X.Z., W.B.M., T.T., X.F., and C.-W.K. conducted the experiments. J.D.H., C.-W.K., and X.Z. designed the experiments. X.Z., C.-W.K., and J.D.H. wrote the manuscript. All authors reviewed and approved the article.

DECLARATION OF INTERESTS

J.D.H. is a consultant for AbbVie and insitro.

505 # Figure Legends

506 ## Figure 1. Identification of the lipogenic complex in liver

507 (A) An adenovirus expressing S14-Flag was injected into mice, and liver lysates were prepared 3
508 days later. Immunoprecipitation was performed using anti-Flag antibodies. Eluates from the S14-
509 Flag IP and an identically processed β-gal–injected control were separated on 8% and 15% SDS–
510 PAGE gels, followed by silver staining. Protein bands that appeared specifically in the S14-Flag
511 lanes were excised and analyzed by LC–MS/MS to identify potential S14-associated proteins.

512 (B) Primary hepatocytes were prepared from rats refed a FFD and plated on collagen-coated
513 coverslips. Immunofluorescence confocal imaging was performed as described in Methods. Co-
514 localization of ACC1 with MIG12 and S14 was confirmed by confocal microscopy using anti-
515 mouse monoclonal ACC1, anti-MIG12 rabbit polyclonal antibodies, and anti-S14 rabbit polyclonal
516 antibodies. Quantitative co-localization analysis was performed using Pearson's correlation
517 (above Costes threshold), and full analytical metrics, including Manders' coefficients and Costes
518 significance testing, are provided in Figure S1 and Supplemental Table 1.

519 ## Figure 2. Co-localization of proteins involved in lipogenesis around LDs in
520 hepatocytes

521 (A) Co-localization of enzymes involved in lipogenesis in primary hepatocytes from rats refed a
522 FFD using confocal microscopy as described in Methods. Quantitative co-localization analysis
523 was performed using Pearson's correlation (above Costes threshold), and full analytical metrics
524 are provided in Supplemental Table 2.

525 (B) Localization of enzymes involved in lipogenesis around LDs in primary hepatocytes from rats
526 refed a FFD using confocal microscopy as described in Methods. Co-localization analysis was
527 performed using Pearson's correlation as in panel A, with results summarized in Supplemental
528 Table 2.

529 (C) A three-dimensional image stack was acquired using an OMX microscope (z-step size: 120
530 nm) to visualize the indicated proteins around lipid droplets, as described in Methods.

531 ## Figure 3. Co-localization of proteins involved in lipogenesis at the interface of
532 mitochondria and LDs in hepatocytes

533 (A) Primary hepatocytes were prepared from rats refed a FFD and localization of ACC1 was
534 determined using immunogold-EM. The 1.4 nm nanogold particles were enlarged by gold
535 enhancement for clear visibility. Detailed protocol is described in Methods.

536 (B) Co-localization of ACC1 and FAS around LDs in primary hepatocytes from rats refed a FFD
537 using immunogold-EM. Size of gold particles: ACC1 - 5 nm; FAS - 10 nm.

538 (C) Co-localization of ACC1 and FAS between mitochondria and LDs in primary hepatocytes from
539 rats refed the FFD using immunogold-EM. Size of gold particles: ACC1 - 5 nm; FAS - 10 nm.

540 (D) Subcellular fractionation was performed with liver lysates from rats refed the FFD to isolate
541 LDs as well as mitochondria, microsomes, and cytoplasm. Detailed protocols for the subcellular
542 fractionation are described in Methods. Proteins from each fraction were subjected to SDS-PAGE
543 and immunoblot analysis with the indicated antibodies. PLIN2, prohibitin, and α-tubulin were used
544 as subcellular localization markers for lipid droplets, mitochondria, and cytosolic proteins,
545 respectively.

546 **Figure 4. Active dephosphorylated ACC promotes polymerization, enhances**
547 **lipogenesis, and increases LD localization**

548 (A) Primary hepatocytes from rats refed a FFD were treated with 1 mM AICAR for 0, 1.5, and 3
549 hours. Equal aliquots of cell lysate proteins were loaded and analyzed by BN-PAGE (above) or
550 SDS-PAGE (bottom) for immunoblot analysis. An anti-ACC1 antibody was used to perform the
551 immunoblot analysis of BN-PAGE. For SDS-PAGE, ACC immunoblots were performed using a
552 fluorescently labeled streptavidin conjugate.

553 (B) Primary hepatocytes from rats refed a FFD were isolated. One set of primary hepatocytes
554 were untreated, while the other two sets were infected with an adenovirus expressing MIG12.
555 After 12 hours, 1 mM AICAR was added, and cells were harvested 3 hours later. Cell lysates were
556 prepared and subjected to BN-PAGE and SDS-PAGE for immunoblot analysis. An anti-ACC1
557 antibody was used to perform the immunoblot analysis of BN-PAGE. For SDS-PAGE, a
558 fluorescently labeled streptavidin conjugate to detect ACC and an anti-MIG12 antibody were used
559 for immunoblot analysis.

560 (C) Primary rat hepatocytes prepared as in (B) were incubated with 1 mM AICAR for 30 minutes
561 and FA synthesis rates were measured *ex vivo* using ^{3}H-acetate as described in Methods.
562 Individual data points are shown; bars indicate the mean (n = 2 technical replicates from one
563 hepatocyte preparation).

564 (D) Liver cytosol from rats refed a FFD were pre-incubated with 1 mM $MnCl_2$ in the presence or
565 absence of a phosphatase inhibitor cocktail for 15 min at 30°C, then incubated with the indicated
566 concentrations of Na-citrate buffer (pH 7.1) for 15 min at 37°C. Palmitate synthesis (left) was
567 measured using ^{14}C-citrate. Palmitate synthesis rates (right) were calculated from the maximal
568 velocity (Vmax) of the enzymatic reaction. Data represent mean ± SEM from n = 3 technical
569 replicates. Statistics: multiple two-tailed unpaired Student's t-tests with Holm–Šidák correction,
570 comparing phosphatase inhibitor–treated (phosphorylated) vs untreated (dephosphorylated)
571 conditions at each citrate concentration (*P < 0.05, **P < 0.01, ***P < 0.001, ****P < 0.0001). The
572 detailed protocol for the enzymatic assay is described in Methods.

573 (E) Rat primary hepatocytes were isolated from rats fed a FFD for 2 days and incubated in medium
574 containing either (i) 25 mM glucose, 100 nM insulin, and 1% DMSO or (ii) 5 mM glucose and 1
575 mM AICAR. Following the indicated times, cells were stained with anti-ACC1 antibodies and
576 LipidTOX as described in Methods.

577 **Figure 5. The interaction of ACC1 with lipid synthesis-associated proteins is**
578 **enhanced when ACC is in the activated state**

579 (A) Liver lysates from refed mice were treated with or without a phosphatase inhibitor cocktail.
580 The ACC1 antibody was incubated with the lysate for 1 hour at RT and ACC1 was
581 immunoprecipitated. IgG was used as the control. The immunoprecipitation protocol is described
582 in Methods. Supernatant indicates the unbound fraction collected after bead pelleting; it was
583 mixed with SDS sample buffer and immunoblotted alongside the bead-bound material.

584 (B) ACC1 immunoprecipitation was carried out using lysates prepared from refed wild-type, ACC1
585 hepatocyte knockout, or ACC2 hepatocyte knockout mouse livers, respectively.

586 **Figure 6. Lipogenic metabolon formation facilitates FA synthesis**

587 (A) Human C-terminal His-Flag-tagged ACSS2, ACL, ACC1, FAS, MIG12, and S14 were
588 individually overexpressed in mammalian HEK 293S GnTI$^-$ cells and purified using Ni-NTA and
589 gel filtration. Epitope tags were removed by TEV cleavage. Detailed protocols for purification were
590 described in Methods. The final purified recombinant proteins were subjected to SDS-PAGE for
591 Coomassie blue staining.

592 (B) Recombinant protein mixtures were incubated with λ-phosphatase and 1 mM $MnCl_2$ for 30
593 minutes at 30°C and then the protein mixture was incubated with 0.5 mM Na-citrate buffer for 20
594 minutes at 30°C. rACC1 was immunoprecipitated from the protein mixture using an anti-ACC1

595 antibody. Recombinant protein mixtures without rACC1 were used for control
596 immunoprecipitations. Proteins were subjected to SDS-PAGE for immunoblot analysis. ACC1
597 immunoblots were performed using a fluorescently labeled streptavidin conjugate.

598 (C) Enzymatic activity of reconstituted recombinant lipogenic enzyme modules was measured as
599 described in Methods. The left panel shows FA synthesis activity measured from citrate using
600 rACL–rACC1–rFAS, whereas the right panel shows FA synthesis activity measured from acetate
601 using rACSS2–rACC1–rFAS. Reactions were performed under phosphorylated or
602 dephosphorylated conditions as indicated. Data represent mean ± SEM from n = 3 technical
603 replicates. Relative synthesis rates were calculated based on Vmax values.

604 (D–E) Under dephosphorylated (D) or phosphorylated (E) conditions, ACL–ACC1–FAS activity
605 was measured in mixtures of liver cytosol (from FFD-refed rats) and recombinant proteins (rACL,
606 rACC1, and rFAS) and compared with the expected additive activity calculated from assays
607 performed in cytosol alone and recombinant proteins alone in parallel. Data represent mean ±
608 SEM from n = 3 technical replicates. Statistical analysis was performed using two-way ANOVA,
609 revealing a significant interaction between phosphorylation state and mixing condition. Post hoc
610 comparisons indicate that observed activity significantly exceeded the expected additive activity
611 only under dephosphorylated conditions. *P < 0.05, **P < 0.01, ***P < 0.001, ****P < 0.0001.

612 (F) Primary hepatocytes isolated from rats under refed or fasted conditions were fixed and stained
613 for ACC1 and β-tubulin, followed by confocal microscopy as described in Methods. Images show
614 representative localization patterns under each condition.

615 (G) Primary hepatocytes from FFD-fed rats were cultured for 8 hours and then treated with DMSO,
616 nocodazole, or taxol (20 μM) as indicated. Cells were subsequently incubated with ^{14}C-labeled
617 citrate for 2 or 4 hours, and citrate-derived FA synthesis was quantified as described in Methods.
618 Data points represent individual measurements from duplicate experiments.

619 **Figure 7. ACC1 anchors a multi-module lipogenic network integrating translation,**
620 **trafficking, and lipid metabolism**

621 (A) Liver lysates were prepared from *ob/ob* mouse livers and ACC1/ACC2–deleted *ob/ob* mouse
622 livers as described in Methods. To activate endogenous phosphatases, lysates were incubated
623 in 5 mM $MgCl_2$ for 30 minutes at 30°C. In parallel, anti-ACC1, anti-MIG12, anti-S14, or anti-
624 ACSS2 antibodies were pre-bound to protein G magnetic beads by incubating for 30 minutes at
625 room temperature. The activated lysates were then added directly to the antibody–bead

626 complexes and incubated for 1 hour at room temperature to perform immunoprecipitation. After
627 extensive washing, bound proteins were eluted by boiling and analyzed by SDS-PAGE and
628 immunoblot analysis was carried out with the indicated antibodies.

629 (B) Proteins co-immunoprecipitated with ACC1, MIG12, or S14 that were reduced by >20-fold in
630 ACC-deficient lysates were classified as ACC1-dependent interactors and subjected to STRING
631 network analysis. Three major functional clusters emerged—translation (red), protein
632 trafficking/transport and cytoskeletal protein binding (green), and FA metabolism (blue). These
633 clusters are displayed both as a network graph and summarized in the bar graph below using the
634 corresponding color scheme. The inset mini-graphs within each colored bar summarize
635 representative GO/KEGG terms for that cluster, with full enrichment analyses provided in Figure
636 S7.

637

638 ## Key resource table

REAGENT or RESOURCE	SOURCE	IDENTIFIER
Antibodies		
Rabbit anti-ACL	Abcam	Cat# ab40793
Rabbit anti-ACSS2	Abcam	Cat# ab66038
Rabbit anti-mouse ACC1	House antibodies[71]	508D or 510D
Mouse monoclonal anti-mouse ACC1	House antibodies	2B5
Rabbit anti-mouse ACC2	House antibodies	456D
Rabbit anti-human FAS	House antibodies	310D
Rabbit anti-mouse MIG12	House antibodies[72]	143D
Mouse monoclonal anti-mouse MIG12	House antibodies	6C4
Rabbit anti-mouse S14	House antibodies	39C
Rabbit anti-PEPCK	Abcam	Cat# ab70358
Mouse anti-β-Tubulin	ThermoFisher	Cat# MA5-16308
Rabbit anti-β-Actin	Cell Signaling	Cat# 4970S
Rabbit Anti-mouse GPAM	House antibodies	280D
Mouse monoclonal anti-rat GPAM	House antibodies	16F8
Anti-ADRP	Sigma	Cat# SAB4200452
Anti-SCD1	Cell Signaling	Cat# 2794S
Anti-PROHIBITIN	Santa Cruz	Cat# SC-56467

Anti-CYTOCHROME C	Millipore	Cat# MAC1800
Mouse anti-CPT1	Abcam	Cat# ab128568
Anti-Ser79-pACC1	Cell Signaling	Cat# 3661S
Anti-PDI	Cell Signaling	Cat# 2446S
Goat Anti-Rabbit IgG, F(ab')2	Jackson Immuno	Cat# 111-035-047
Goat Anti-Mouse IgG, F(ab')2	Jackson Immuno	Cat# 115-035-072
Li-COR IRDye 800 goat anti-Rabbit IgG	Fisher Scientific	Cat# NC9401842
Li-COR IRDye 680 goat anti-Mouse IgG	Fisher Scientific	Cat# NC0252290
Li-COR IRDye 680RD Streptavidin	Fisher Scientific	Cat# NC0337633
Bacterial and virus strains		
Stellar™ Competent Cells	Takara	Cat# 636764
TOP10 Competent Cells	ThermoFisher	Cat# C404003
Chemicals, peptides, and recombinant proteins		
LB broth	Research Products International	Cat# L24061
Freestyle 293 expression medium	Gibco	Cat# 12338018
Opti-MEM™ I Reduced Serum Medium	Gibco	Cat# 31985070
Fetal Calf Serum (FCS)	Sigma-Aldrich	Cat# F2442
Penicillin-Streptomycin solution (100x)	Corning	Cat# 30-002-CI
PEI 25K	Polysciences	Cat# 23966-1
Protease Inhibitor Cocktail Set III, EDTA-Free - Calbiochem	Millipore-Sigma	Cat# 539134-1ML
Protease Inhibitor Cocktail, for use in purification of Histidine-tagged proteins, DMSO solution	Sigma-Aldrich	Cat# P8849-5ML
Purified rTEV protease	Gift from Dr. Jinhai Yu, UT Southwestern Medical Center	N/A
Lambda Protein Phosphatase	New England Biolabs	Cat# P0753L
DL-Dithiothreitol	Sigma-Aldrich	Cat# 43819-5G
Adenosine 5'-triphosphate magnesium salt	Sigma-Aldrich	Cat# A9187-1G
Adenosine 5'-triphosphate disodium salt hydrate	Sigma-Aldrich	Cat# A2383-5G

Coenzyme A sodium salt hydrate	Sigma-Aldrich	Cat# C3144-25MG
Acetyl coenzyme A sodium salt	Sigma-Aldrich	Cat# A2056-25MG
Malonyl coenzyme A lithium salt	Sigma-Aldrich	Cat# M4263-10MG
NADPH, Tetrasodium Salt	Sigma-Aldrich	Cat# 481973-100MG
Sodium bicarbonate [14C]	American Radiolabeled Chemicals	Cat# ARC 0138C-50 µCi
Malonyl [2-14C] Coenzyme A	American Radiolabeled Chemicals	Cat# ARC 0528-25 µCi
Citric Acid, [1,5-14C]	Revvity	Cat# NEC160050UC
Acetic Acid, Sodium Salt, [1,2-14C]	Revvity	Cat# NEC553050UC
Lauryl Maltose Neopentyl Glycol	Anatrace	Cat# NG310 5 GM
3a70B Complete Counting Cocktail	Research Products International	Cat# 111154
In-Fusion® Snap Assembly Value Bundle	Takara	Cat# 638946
Platinum™ SuperFi II PCR Master Mix	ThermoFisher	Cat# 12368010
DreamTaq Green PCR Master Mix (2X)	ThermoFisher	Cat# K1081
Oleoyl coenzyme A dipotassium salt	ThermoFisher	Cat# CN10090405
sn-Glycerol 3-phosphate lithium salt	Sigma-Aldrich	Cat# 94124-10MG
Glycerol, L-[14C(U)] 3-phosphate disodium salt	American Radiolabeled Chemicals	Cat# ARC 0316-50 µCi
Sodium butyrate	Sigma-Aldrich	Cat# 303410-500G
HCS LipidTOX™ Deep Red Neutral Lipid Stain, for cellular imaging	Fisher Scientific	Cat# H34477
Clean-Blot™ IP Detection Reagent (HRP)	Thermo Scientific	Cat# 21230
AICAR	Abcam	Cat# ab120358
Critical commercial assays		
Pierce™ Coomassie (Bradford) Protein Assay Kit	ThermoFisher	Cat# 23200

Pierce BCA Protein Assay Kit	ThermoFisher	Cat# 23225
Silver staining Kit	ThermoFisher	Cat# 24612
Experimental models: Cell lines		
HEK-293S GnTI$^-$	ATCC	Cat# CRL-3022; RRID: CVCL_A785
CHO-K1	ATCC	Cat# CCL-61; RRID: CVCL_0214
Experimental models: Organisms/strains		
C57BL/6J mouse	Jackson Laboratory	Stock# 000664
ob/ob mouse	Jackson Laboratory	Stock# 000632
Sprague Dawley	Charles River	SAS SD code 400
Phosphatase inhibitor cocktail		
Sodium Fluoride	Sigma-Aldrich	Cat# S7920
Imidazole	Sigma-Aldrich	Cat# I5513
Sodium molybdate	Sigma-Aldrich	Cat# M1003
Sodium tartrate dihydrate	Sigma-Aldrich	Cat# S4797
Sodium pyrophosphate	Sigma-Aldrich	Cat# P8135
β-glycerophosphate	Sigma-Aldrich	Cat# G9422
Recombinant DNA		
pEZT-BM	Addgene	Plasmid #74099
ATP citrate lyase (ACLY) (NM_001096) Human Tagged ORF Clone	Origene	Cat# RC200508
ACSS2 (NM_018677.4) cDNA ORF clone, Homo sapiens (human)	Genscript	Cat# OHu18043
ACL-Tev-Flag-His-XT3	IDT DNA	N/A
ACC1-Tev-Flag-His-XT3	IDT DNA	N/A
FAS-Tev-Flag-His-XT3	IDT DNA	N/A
MIG12-Tev-Flag-His_Human	IDT DNA	N/A
S14-Tev-Flag-His_Human	IDT DNA	N/A
PEPCK_Human-Tev-His	IDT DNA	N/A
pEZT-BM-ACL-3xFlag-10xHis	This paper	N/A
pEZT-BM-ACSS2-3xFlag-10xHis	This paper	N/A
pEZT-BM-ACC1-3xFlag-10xHis	This paper	N/A

pEZT-BM-FAS-3xFlag-10xHis	This paper	N/A
pEZT-BM-MIG12-3xFlag-10xHis	This paper	N/A
pEZT-BM-S14-3xFlag-10xHis	This paper	N/A
pEZT-BM-PEPCK-3xFlag-10xHis	This paper	N/A
ACC1-pcDNA3.1	This paper	N/A
ACC2-pcDNA3.1	This paper	N/A
Software and algorithms		
Image Studio™ Version 5.0	Li-COR	N/A
Prism 10	GraphPad	https://www.graphpad.com/
Adobe Illustrator 2023	Adobe	N/A
Other		
PD-10 desalting columns	Cytiva	Cat# 17085101
Superose 6 10/300 GL column	Cytiva	Cat# GE17-5172-01
Amicon Ultra centrifugal filter	Millipore	Cat# UFC903008
Ni-NTA Resin	Thermo Scientific	Cat# 88221
Slide-A-Lyzer dialysis cassette	Thermo Scientific	Cat# 66203
Dynabeads Protein A beads	Invitrogen	Cat# 10002D
Scintillation vials	Research Products International	Cat# 121040
Disposable Round-Bottom Rimless Glass Tubes	Corning	Cat# 14-962-15E
4–15% Criterion™ TGX™ Precast Midi Protein Gel, 26 well, 15 µl	BIO-RAD	Cat# 5671085
4–15% Mini-PROTEAN® TGX™ Precast Protein Gels, 15-well, 15 µl	BIO-RAD	Cat# 4561086
Dynabeads™ Protein G for Immunoprecipitation	Fisher Scientific	Cat# 10-004-D
Slide Warmer (110 V, for 23 slides)	Fisher Scientific	Cat# 50-930-986

Methods

Experimental model and study participant details

Animals and primary hepatocytes

643 Primary hepatocytes were isolated from 4-week-old male Sprague–Dawley rats fasted for 12
644 hours and refed for 12 hours with a fat-free diet, using collagenase perfusion as described by
645 Shimomura et al. [73] All rat studies were performed under an approved protocol from the UT
646 Southwestern Institutional Animal Care and Research Advisory Committee (IACUC #2015-
647 100838). Liver tissues were collected from wild-type male C57BL/6 mice, liver-specific ACC1
648 and/or ACC2 knockout male C57BL/6 mice, or ob/ob male C57BL/6 mice. All mice were
649 maintained under standard housing conditions with a 12-hour light/dark cycle (lights on at 6 AM
650 and off at 6 PM). Mouse studies were conducted under UT Southwestern IACUC approval (2015-
651 101135-G). Nocodazole and taxol were used at 20 μM to achieve robust disruption or stabilization
652 of microtubules, respectively, in primary hepatocytes.

653 **Method Details**

654 **Antibody generation**

655 For the generation of the mouse monoclonal antibody that recognizes mouse ACC1, a cDNA
656 encoding the N-terminal 95 amino acids of mouse ACC1 was cloned into a pGEX-4T-1 vector
657 and the recombinant protein was expressed in *Escherichia coli (E. coli)* and purified using
658 glutathione agarose. Monoclonal antibodies were generated by fusion of Sp2/mIL-6 (CRL-2016;
659 ATCC) mouse myeloma cells with splenic B lymphocytes derived from a female NZBWF1/J
660 mouse injected with purified mouse ACC1 protein [74,75].

661 For the generation of a rabbit polyclonal antibody against mouse ACC2, a cDNA encoding the N-
662 terminal 200 amino acids of mouse ACC2 was cloned into a pRSF-1b expression vector and
663 expressed in *E. coli*. The purified His-tagged protein was isolated using nickel affinity resin and
664 injected into rabbits as described [76].

665 For the generation of rabbit polyclonal antibody against human FAS, a cDNA encoding the C-
666 terminal 305 amino acids from human FAS was cloned into pGEX-4T-1 expression vector and
667 expressed in *E. coli.* The purified GST-fusion protein was injected into rabbits as described [19].

668 For the generation of a rabbit polyclonal antibody against mouse S14, recombinant (His)6-mouse
669 S14 was expressed in E. coli, purified by Ni-NTA affinity chromatography (Qiagen) according to
670 the manufacturer's protocol, and injected into rabbits as described [19].

671 For the generation of rabbit polyclonal antibody against mouse GPAM, a cDNA encoding the N-
672 terminal 150 amino acids from mouse GPAM was cloned into pRSF-1b expression and expressed
673 in *E. coli*. The purified His-tagged protein was injected into rabbits as described [19].

674 For the generation of mouse monoclonal antibody against rat GPAM, a cDNA encoding amino
675 acids 627 to 717 of rat GPAM was cloned into pRSF-1b expression vector and expressed in *E.*
676 *coli*. The purified His-tagged protein was injected into mice, and monoclonal antibodies were
677 produced as described above. For the generation of mouse monoclonal antibody against mouse
678 MIG12, full length mouse MIG12 cDNA was cloned into pRSF-1b and expressed in *E. coli* and
679 the purified protein (Ni-NTA agarose) was injected into mice. Monoclonal antibodies were
680 generated using the same hybridoma fusion strategy described for ACC1.

681 **Immunofluorescence**

682 Primary hepatocytes from refed rat livers were fixed in 4% paraformaldehyde (PFA) in PHEM
683 buffer (pH 7.4) for 30 minutes. After rinsing the cells with 0.1 M phosphate buffer, they were
684 permeabilized with pre-chilled (−20°C) methanol for 15 min at −20°C. Blocking was performed
685 using 1% BSA and 0.2% fish skin gelatin in 0.1 M phosphate buffer (pH 7.4) for 30 minutes at
686 room temperature. Primary antibodies were incubated overnight at 4°C in the blocking solution,
687 and Alexa Fluor 488- or 568-labeled secondary antibodies were used to visualize the localization
688 of each target protein. Imaging was conducted using a Zeiss LSM880 Airyscan microscope.

689 **Colocalization analysis**

690 Colocalization was quantified using the Coloc2 plugin in Fiji/ImageJ. To minimize background
691 noise and evaluate biologically relevant signal overlap, analysis was performed on lipid droplet–
692 enriched regions, which represent functional sites of lipogenic enzyme accumulation. CZI files
693 were imported directly into Fiji, and channels were split and processed separately to avoid
694 spectral bleed-through. Images used for Coloc2 analysis were converted to 8-bit format prior to
695 computation. Pearson's correlation coefficients were calculated using Costes automatic
696 thresholding, and above-threshold Pearson's R values were reported in the main text.
697 Thresholded Manders' coefficients (tM1 and tM2), Costes significance testing, and 2D intensity
698 histograms were generated by Coloc2 and are presented in Figure S1. All images were acquired
699 below saturation, identical ROIs were applied to paired channels for each analysis.

700 **Pre-embedding immuno-electron microscopy**

701 Primary hepatocytes from refed rat livers were fixed in 4% PFA/0.05% glutaraldehyde (GA) in
702 PHEM buffer (pH 7.4) for 30 minutes. After rinsing the cells with 0.1 M phosphate buffer, residual
703 aldehydes were quenched with 50 mM glycine in 0.1 M phosphate buffer for 15 minutes, followed
704 by permeabilization with 0.2 mg/mL saponin for 30 minutes at room temperature. Blocking was

705 performed using 5 μg/mL saponin, 1% BSA, 0.2% fish skin gelatin, and 5% goat serum in 0.1 M
706 phosphate buffer (pH 7.4) for 15 minutes at room temperature. The primary antibody was
707 incubated overnight at 4°C in the blocking solution. After incubation, cells were labeled with an
708 anti-rabbit or anti-mouse IgG secondary antibody conjugated to 1.4 nm gold. Following post-
709 fixation, the samples were subjected to gold enhancement, embedded in Embed-812 resin, and
710 cut into 60 nm sections. Electron micrographs were taken using the TEM JEOL 1400 Plus
711 microscope. For ACC1 and FAS double immunogold labeling, ACC1 and FAS primary antibodies
712 were bound to 5 nm and 10 nm colloidal gold-conjugated secondary antibodies, respectively. After
713 post-fixation, the cells were embedded in Embed-812 resin, sectioned into 60 nm slices, and
714 imaged using the JEOL 1400 Plus Transmission Electron Microscope. The pre-embedding
715 method followed the procedure described by Yamamoto *et al*. [77]

716 **Liver subcellular fractionation**

717 Fresh rat or mouse liver was homogenized in 50 mM Tris (pH 7.4) and 250 mM sucrose in the
718 presence of protease inhibitors. For lipid droplet isolation, half of the homogenate was transferred
719 to a new tube, and buffer A (20 mM HEPES, pH 7.4, 100 mM KCl, 2 mM $MgCl_2$) was gently added
720 to the top. The sample was centrifuged at 2,000 × g for 30 minutes, and the floating lipid layer
721 was transferred to a new tube. This lipid layer was mixed with an equal volume of buffer A-500S
722 (20 mM HEPES, pH 7.4, 100 mM KCl, 2 mM $MgCl_2$, and 500 mM sucrose) and gently overlaid
723 with buffer A. This step was repeated twice to isolate a pure lipid layer. A glass pipette was used
724 during lipid layer purification to minimize loss of lipid. Proteins from the lipid layer were extracted
725 using an organic solvent as described [78] and resuspended in SDS-lysis buffer (50 mM Tris, pH
726 6.8, 50 mM NaCl, 1% SDS). For mitochondria and microsome fractionations, the remaining half
727 of the liver homogenate was centrifuged at 1,000 × g for 10 minutes to remove the nuclear fraction.
728 The supernatant was centrifuged at 10,000 × g for 20 minutes to pellet the mitochondrial fraction.
729 The mitochondrial pellet was resuspended and washed twice more with homogenization buffer
730 by repeated centrifugation at 10,000 × g for 20 minutes. The final mitochondrial pellet was
731 resuspended in SDS-lysis buffer. The supernatant from the 10,000 × g centrifugation was further
732 centrifuged at 100,000 × g for 30 minutes to sediment the microsomal fraction, which contains the
733 endoplasmic reticulum. The microsomal pellet was rinsed with homogenization buffer and
734 resuspended in SDS-lysis buffer.

735 **Recombinant protein expression and purification**

736 **Expression**

737 The cDNAs encoding human ACSS2, ACL, ACC1, FAS, MIG12, S14, and PEPCK were cloned
738 into the pEZT-BM vector containing a TEV protease cleavage site, an SSG linker, followed by a
739 C-terminal 3 × Flag tag and 10 × His tag. All proteins were expressed in mammalian HEK 293S
740 GnTI⁻ cells (ATCC). A total of 500 mL of HEK 293S GnTI⁻ cells were transfected at a density of
741 2–3 × 10^6 cells/mL with 0.75 mg of plasmid DNA using PEI 25K (Polysciences). 16 hours post-
742 transfection, 250 mL of Freestyle 293 expression medium (Gibco) supplemented with 2% fetal
743 calf serum (FCS) and 1% penicillin-streptomycin solution (Corning) was added to the cultures.
744 Sodium butyrate was added to a final concentration of 8 mM to enhance protein expression. Cells
745 were harvested 72 hours post-transfection for subsequent protein purification.

746 **Purification**

747 The cell pellet from 400 mL culture was resuspended and homogenized in 100 mL buffer B (50
748 mM phosphate buffer, 500 mM NaCl, 1 mM DTT, 5 mM imidazole, 225 mM mannitol, 75 mM
749 sucrose, protease inhibitor cocktail (Millipore-Sigma), protease inhibitor cocktail for use in
750 purification of Histidine-tagged proteins (Sigma-Aldrich), pH 8.0). The homogenate was
751 centrifuged at 135,000 × g for 45 minutes at 4 °C. The supernatant was collected and filtered
752 through a 5 μm filter. The filtered supernatant was loaded on a 2 mL Ni-NTA resin (Thermo
753 Scientific) that pre-equilibrated with buffer B and flowed through by gravity (~1 ml/min) at 4°C.
754 The Ni-NTA was then washed sequentially with 10 CV buffer B and 25 CV buffer C (50 mM
755 phosphate buffer, 500 mM NaCl, 1 mM DTT, 50 mM imidazole, 10% glycerol, pH 8.0) by gravity.
756 Proteins were eluted in 5 CV buffer D (50 mM phosphate buffer, 500 mM NaCl, 1 mM DTT, 500
757 mM Imidazole, 10% glycerol, pH 8.0). The eluate was desalted using a PD-10 desalting column
758 (Cytiva) pre-equilibrated with buffer E (10 mM HEPES, 50 mM NaCl, 100 mM KCl, 1 mM DTT, 5%
759 glycerol, pH 7.4). Proteins were eluted in buffer E and incubated with TEV protease overnight at
760 4 °C.

761 **Removal of TEV and tags**

762 rACL, rACC1, and rFAS: the TEV-cleaved proteins were concentrated to 0.5 mL using a 30,000
763 MWCO Amicon Ultra centrifugal filter (Millipore) and then subjected to gel-filtration
764 chromatography on a Superose 6 10/300 GL column (Cytiva) pre-equilibrated with buffer E.
765 Purified proteins eluted as a single sharp peak in buffer E. Protein homogeneity was confirmed
766 by Coomassie blue-stained SDS-PAGE.

767 rACSS2, rMIG12, rS14, and rPEPCK: the TEV-cleaved proteins were loaded on 2 mL Ni-NTA
768 resin and flowed through by gravity (~1 ml/min) pre-equilibrated with buffer E. The Ni-NTA resin

769 was then washed sequentially with 5 CV buffer B, 5 CV buffer C and 5 CV buffer D by gravity
770 flow. The flow-through and eluted fractions without His tag signal were combined and
771 concentrated using an Amicon Ultra centrifugal filter (Millipore) (rACSS2 and rPEPCK: 30,000
772 MWCO, rMIG12: 10,000 MWCO, rS14: 3,000 MWCO) and then dialyzed using a 2,000 MWCO
773 Slide-A-Lyzer dialysis cassette (Thermo Scientific) in 2 L buffer E overnight at 4°C.

774 **Co-immunoprecipitation of recombinant proteins**

775 Recombinant ACC1, FAS, ACL, ACSS2, MIG12, S14, and PEPCK were mixed at 8: 64: 20: 40:
776 32: 96: 1 molar ratios, respectively. Groups lacking recombinant ACC1 served as controls. The
777 protein mixtures were incubated with 40 mM HEPES (pH 7.1), 1 mM $MnCl_2$, and λ-phosphatase
778 (New England Biolabs) for 30 minutes at 30°C. For phosphorylated groups, the mixtures were
779 incubated with a phosphatase inhibitor cocktail instead of lambda phosphatase, under the same
780 conditions. The reaction systems were then supplemented with 0.5 mM Na-citrate buffer (pH 7.1)
781 and incubated for 20 minutes at 30°C.

782 After pre-incubation, 5 μg of ACC1 polyclonal antibody was added to each reaction and incubated
783 for an additional 10 minutes at 30°C. Buffer F (50 mM NaCl, 100 mM KCl, 20 mM HEPES, 4 mM
784 $MgCl_2$, 1% LMNG, pH 7.1) was added, and the mixtures were incubated with rotation for 1 hour
785 at room temperature. Subsequently, 25 μL Dynabeads Protein A (Invitrogen) were added and
786 incubated with rotation for 20 minutes at room temperature. The beads were washed four times
787 with buffer F. Bound proteins were eluted by incubation with 1× SDS sample buffer for 10 minutes
788 at 95°C. Eluted proteins were analyzed by immunoblot analysis using the indicated antibodies.

789 **Co-immunoprecipitation of liver lysates**

790 Liver slices from fresh mouse (or rat) livers were homogenized in 10 mM Tris (pH 7.1), 250 mM
791 sucrose, and 1% LMNG (Lauryl maltose neopentyl glycol) in the presence of protease inhibitors.
792 The homogenate was centrifuged at 25,600 × g for 15 minutes at 20°C. The supernatant was
793 collected and filtered through a 0.45 μm filter. The clarified supernatant was divided into two tubes;
794 5 mM $MgCl_2$ was added to both, whereas phosphatase inhibitor cocktail was added to only one.
795 After incubation at 30°C for 30 minutes, NaCl and KCl were added to final concentrations of 50
796 mM and 100 mM, respectively. Mouse monoclonal ACC1 antibody or mouse IgG control antibody
797 was added to each tube, and the samples were incubated for 1 hour at room temperature.
798 Dynabeads Protein G (25 μL) were then added and incubated for a further 25 minutes at room
799 temperature. The beads were washed 5 times with 10 mM Tris (pH 7.1), 100 mM KCl, 50 mM

800 NaCl, 5 mM $MgCl_2$, and 1% LMNG. The beads were boiled in SDS-loading buffer for 5 minutes
801 to elute proteins co-immunoprecipitated with ACC1.

802 Mass Spectrometry

803 Immunoprecipitates were resolved by SDS–PAGE, Coomassie-stained, and the excised gel
804 regions were submitted to the UT Southwestern Proteomics Core Facility for LC–MS/MS analysis.
805 Protein identification and label-free quantification were performed using the core's standard
806 Complex Mixture ID workflow, and processed datasets were used for downstream analyses.

807 Radiometric FA synthesis in hepatocytes

808 Rat primary hepatocytes were cultured in 6-well dishes coated with collagen. Where indicated,
809 after 8 hours of culture, cells were treated with DMSO, nocodazole, or taxol (20 μM). On the day
810 of study, the culture medium was replaced with medium containing 1 mM acetate or citrate,
811 supplemented with 1 μCi [^{14}C]-labeled acetate or citrate, respectively, and cells were harvested
812 after the indicated incubation times by adding 1 mL of 0.1 N NaOH. A recovery carrier (^{3}H oleic
813 acid), 1.5 mL of ethanol, and 0.75 mL of 75% KOH were added to the harvested cells, and the
814 mixture was autoclaved for 45 minutes on slow exhaust for saponification. After saponification,
815 1.5 mL of ethanol and 1.5 mL of HCl were added sequentially with vigorous vortexing. After
816 cooling, 1.5 mL of ethanol was added, and fatty acids were extracted three times with 3 mL of
817 hexane. The solvent was evaporated under nitrogen, and the residue was re-dissolved in 30 μL
818 of chloroform. Samples were spotted onto plastic-backed silica gel TLC plates and resolved in a
819 solvent system consisting of heptanes:diethyl ether:acetic acid (90:30:1, v/v/v). After visualization
820 with iodine vapor, each FA spot was excised and radioactivity was quantified by scintillation
821 counting. FA synthesis was calculated based on the recovered radioactivity.

822 Recombinant protein enzyme assays

823 Dephosphorylation treatment

824 Different recombinant proteins were pre-incubated with 20 mM HEPES (pH 7.1), 1 mM $MnCl_2$,
825 and lambda phosphatase for 30 minutes at 30°C in 96 well plates (Corning). The same groups
826 without lambda phosphatase were used as phosphorylated groups.

827 ACSS2 and ACL (LC-MS/MS)

828 For the ACL activity assay, protein samples from dephosphorylation treatment were incubated at
829 37°C in a reaction mixture containing 20 mM HEPES (pH 7.1), 1 mM DTT, 1 mg/mL BSA, 4 mM
830 sodium citrate (pH 7.1), 5 mM Mg-ATP (pH 7.1), and 0.1 mM CoA. For the ACSS2 activity assay,
831 protein samples were incubated at 37°C with 20 mM HEPES (pH 7.1), 1 mM DTT, 1 mg/mL BSA,
832 4 mM sodium acetate (pH 7.1), 5 mM Mg-ATP (pH 7.1), and 0.1 mM CoA. At designated time
833 points (0, 4, 8, 16, and 32 minutes), reactions were terminated by the addition of 8 N HCl, followed
834 by thorough mixing. Each sample was then immediately spiked with a [1-^{13}C]acetyl-CoA internal
835 standard prior to further analysis.

836 Samples were centrifuged at 4°C for 10 minutes and 150 µL supernatant was loaded on an Oasis
837 HLB 1cc-30 mg solid-phase extraction column. The column was washed with water and methanol.
838 The eluent was lyophilized and dissolved in 50 µL of mobile phase of which 1 µL was subjected
839 to LC/MS/MS analyses. Analysis was performed on an API 3200 triple quadrupole LC/MS/MS
840 mass spectrometer (Applied Biosystems/Sciex Instruments) in positive electrospray ionization
841 mode. The mass spectrometer was equipped with a Shimadzu LC-20AD liquid chromatograph
842 (LC) and a SIL-20ACHT auto sampler. Chromatography was performed on a reverse-phase C18
843 column (Waters XBridge, 150 x 2.1 mm, 3 µm) with a mobile phase consisting of water/methanol
844 (95:5, v/v) and 4mM dibutylamine acetate (eluent A), and water/acetonitrile (25:75, v/v) (eluent
845 B). Multi-reaction monitoring (MRM) was carried out for the detection of the short-chain acyl-CoAs
846 in standard solutions and biological samples. Acetyl-CoA was quantitated by comparison of the
847 individual ion peak area with that of the internal standard. The analytical data were processed by
848 Analyst Software (version 1.6.2).

849 **ACC1 (radiometric)**

850 Following pre-incubation in dephosphorylation treatment step, rACC1 was incubated at 37°C in a
851 reaction mixture containing 20 mM HEPES (pH 7.1), 1 mM DTT, 1 mg/mL BSA, 5 mM $NaHCO_3$,
852 5 mM Mg-ATP (pH 7.1), 0.25 mM acetyl-CoA, and 0.225 µCi [^{14}C]$NaHCO_3$ (American
853 Radiolabeled Chemicals). At designated time points (0, 4, 8, 16, and 32 minutes), reactions were
854 terminated by the addition of 8 N HCl. The mixtures were transferred to scintillation vials
855 (Research Products International Corp.) and air-dried completely at 100°C. Dried samples were
856 then dissolved in 1 mL of methanol, and [^{14}C] radioactivity was quantified by liquid scintillation
857 counting (Beckman Coulter) following the addition of scintillation cocktail (Research Products
858 International Corp.).

859 **FAS (radiometric)**

860 Following pre-incubation in dephosphorylation treatment step, rFAS was incubated at 37°C in a
861 reaction mixture containing 20 mM HEPES (pH 7.1), 1 mM DTT, 1 mg/mL BSA, 0.1 mM acetyl-
862 CoA, 0.3 mM malonyl-CoA, 0.5 mM NADPH, and 0.02 μCi [^{14}C]malonyl-CoA (American
863 Radiolabeled Chemicals). At designated time points (0, 4, 8, 16, and 32 minutes), reactions were
864 terminated by adding HCl/methanol (6:4, v/v) in 16 × 100 mm glass tubes (Corning). Ethanol and
865 hexane were added at a volume ratio of 1:1:2 (HCl/methanol:ethanol:hexane), and the mixtures
866 were vortexed thoroughly. Samples were centrifuged at 2,000 × g for 5 minutes at room
867 temperature. The upper organic phase was transferred to scintillation vials and air-dried
868 completely at RT. Dried lipids were dissolved in 1 mL of methanol, and [^{14}C] radioactivity was
869 quantified by liquid scintillation counting (Beckman Coulter) following the addition of scintillation
870 cocktail (Research Products International Corp.).

871 **ACL-ACC1-FAS (radiometric)**

872 After pre-incubation in dephosphorylation treatment step, recombinant ACL (0.8 μg), ACC1 (0.4
873 μg), and FAS (3.2 μg) were incubated at 37 °C in a reaction mixture containing 20 mM HEPES
874 (pH 7.1), 1 mM DTT, 1 mg ml^{-1} BSA, 4 mM sodium citrate (pH 7.1), 5 mM $NaHCO_3$, 5 mM Mg-
875 ATP (pH 7.1), 0.1 mM CoA, 1 mM NADPH, and 0.025 μCi [1,5-^{14}C]citric acid (Revvity). At
876 designated time points (0, 4, 8, 16, and 32 minutes), reactions were terminated by adding
877 HCl/methanol (6:4, v/v) in 16 × 100 mm glass tubes (Corning). Ethanol and hexane were added
878 at a volume ratio of 1:1:2 (HCl/methanol:ethanol:hexane), and the mixtures were vortexed
879 thoroughly. Samples were centrifuged at 2,000 × g for 5 minutes at room temperature. The upper
880 organic phase was transferred to scintillation vials and air-dried completely at RT. Dried lipids
881 were dissolved in 1 mL of methanol, and [^{14}C] radioactivity was quantified by liquid scintillation
882 counting (Beckman Coulter) following the addition of scintillation cocktail (Research Products
883 International Corp.).

884 **ACSS2-ACC1-FAS (radiometric)**

885 Following pre-incubation in dephosphorylation treatment step, recombinant ACSS2 (0.4 μg),
886 ACC1 (0.4 μg), and FAS (3.2 μg) were incubated at 37 °C in a reaction mixture containing 20 mM
887 HEPES (pH 7.1), 1 mM DTT, 1 mg ml^{-1} BSA, 4 mM sodium acetate (pH 7.1), 5 mM $NaHCO_3$, 5 mM
888 Mg-ATP (pH 7.1), 0.1 mM CoA, 1 mM NADPH, and 0.0225 μCi [1,2-^{14}C]acetic acid (Revvity). At
889 designated time points (0, 4, 8, 16, and 32 minutes), reactions were terminated by adding
890 HCl/methanol (6:4, v/v) in 16 × 100 mm glass tubes (Corning). Ethanol and hexane were added
891 at a volume ratio of 1:1:2 (HCl/methanol:ethanol:hexane), and the mixtures were vortexed

892 thoroughly. Samples were centrifuged at 2,000 × g for 5 minutes at room temperature. The upper
893 organic phase was transferred to scintillation vials and air-dried completely at RT. Dried lipids
894 were dissolved in 1 mL of methanol, and [^{14}C] radioactivity was quantified by liquid scintillation
895 counting (Beckman Coulter) following the addition of scintillation cocktail (Research Products
896 International Corp.).

897 **Cytosol-based citrate-to-palmitate assay**

898 Mouse livers collected after fasting-refeeding treatment were homogenized in Buffer I (20 mM
899 HEPES, 250 mM sucrose, protease inhibitor cocktail (Millipore-Sigma), pH 7.1) at a liver-to-buffer
900 ratio of 1:5 (w/v). Homogenates were centrifuged at 6,000 × g for 10 minutes at 4 °C. The resulting
901 supernatant was subjected to further centrifugation at 180,000 × g for 60 minutes at 4 °C. The
902 supernatant was then loaded on PD-10 desalting column (Cytiva) that pre-equilibrated with buffer
903 J (20 mM HEPES, 50 mM KCl, 1 mM DTT, and protease inhibitor cocktail (Millipore-Sigma), pH
904 7.1) and flowed through by gravity. Liver cytosols were eluted in buffer J.

905 For pre-incubation, 300 µg of liver cytosol was incubated with 20 mM HEPES (pH 7.1), 1 mM
906 $MnCl_2$, and phosphatase inhibitor cocktail at 30 °C for 15 minutes. Parallel samples without
907 phosphatase inhibitor cocktail served as the dephosphorylated groups.

908 Following pre-incubation, liver cytosol samples were incubated at 37 °C for 15 minutes in a
909 reaction mixture containing 20 mM HEPES (pH 7.1), 5 mM $MgCl_2$, 1 mM DTT, 1 mg ml^{-1} BSA,
910 varying concentrations of sodium citrate (pH 7.1), 5 mM $NaHCO_3$, 5 mM ATP (disodium salt,
911 pH 7.1), 0.1 mM CoA, 1 mM NADPH, and 0.05 µCi [1,5-^{14}C]citric acid (Revvity). Reactions were
912 terminated by adding 1 N HCl/methanol (6:4, v/v) in 16 × 100 mm glass tubes (Corning), followed
913 by vortexing with ethanol and hexane. The final solvent ratio of quenching
914 solution:ethanol:hexane was 1:1:2. Samples were centrifuged at 2,000 × g for 5 minutes at room
915 temperature (RT), and the upper organic phase was collected, transferred to scintillation vials,
916 and air dried completely at RT. Dried lipids were dissolved in 1 mL methanol, and [^{14}C]
917 radioactivity was quantified by liquid scintillation counting (Beckman Coulter) following the
918 addition of scintillation cocktail (Research Products International Corp.).

919 **TG synthesis in liver homogenates**

920 The livers of fasted/refed rats were homogenized in buffer K (10 mM HEPES, 1 mM EDTA, 1 mM
921 DTT, and protease inhibitor cocktail (Millipore-Sigma), pH 7.1) at a tissue-to-buffer ratio of 1:4

922 (w/v). The homogenate was filtered through gauze to remove unbroken tissue and then dialyzed
923 against dialysis buffer (10 mM HEPES, 50 mM KCl, 1 mM DTT, 1 mM PMSF, pH 7.1) for 2 hours.

924 The liver homogenates were pre-incubated with various concentrations of $MgCl_2$ (0, 2.5, 5, 10, 20
925 mM), 4 mM of Na-citrate buffer (pH 7.1), a phosphatase inhibitor cocktail, and 50 mM phosphate
926 buffer (pH 7.1) for 5 minutes at 37°C. Parallel groups without phosphatase inhibitor cocktail and
927 phosphate buffer served as dephosphorylated controls. After pre-incubation, samples were
928 incubated for 30 minutes at 37 °C in a reaction mixture containing 1 mM DTT, 1 mg/mL BSA,
929 10 mM oleoyl-CoA, 100 mM glycerol 3-phosphate, and 0.2 μCi [^{14}C]glycerol 3-phosphate
930 (American Radiolabeled Chemicals). Reactions were terminated by adding 1 N HCl/methanol
931 (6:4, v/v) in 16 × 100 mm glass tubes (Corning). The mixtures were then vortexed with phosphate-
932 buffered saline (PBS) and Folch reagent (chloroform:methanol = 2:1, v/v). The final solvent ratio
933 of HCl/methanol:PBS:Folch was 1:1:3. Samples were centrifuged at 2,000 × g for 5 minutes at
934 room temperature (RT), and the lower organic phases were transferred to new glass tubes and
935 air dried completely at RT. Dried lipids were reconstituted in 50 μL chloroform and vortexed.
936 Extracted lipids, along with a TG marker, were loaded onto thin-layer chromatography (TLC)
937 plates. Plates were developed in a TLC chamber saturated with a solvent system of
938 hexane:diethyl ether:acetic acid (80:20:1, v/v/v). TG dots were visualized using iodine vapor,
939 identified by comparison with the TG marker. TG dots were excised from the plates and
940 transferred to scintillation vials. Scintillation cocktail (Research Products International Corp.) was
941 added to each vial, followed by vortexing. [^{14}C] radioactivity was quantified by liquid scintillation
942 counting (Beckman Coulter).

943 **Enzyme Synergy Assays (Recombinant ± Cytosol)**

944 For dephosphorylation treatment, a mixture containing rACL (0.5 μg), rACC1 (0.25 μg), and rFAS
945 (2 μg) or an equal volume of protein purification buffer (Buffer E) (used for the cytosol only groups)
946 were incubated in a 25 μL total volume system with λ-phosphatase in the presence of 1 mM $MnCl_2$
947 at 30°C for 20 minutes. The resulting 22 μL reaction was combined with 20 μL of liver cytosol
948 (300 μg) or cytosol preparation buffer (Buffer J) (used for the recombinant protein only groups) in
949 a final volume of 50 μL and incubated at 30°C with 5 mM $MgCl_2$ for an additional 20 minutes.

950 To maintain proteins in a phosphorylated state, the same protein mixture or Buffer E was
951 incubated under identical conditions with phosphatase inhibitor cocktail instead of λ-phosphatase.
952 The resulting 22 μL reaction was then mixed with 20 μL of liver cytosol (300 μg) or Buffer J and
953 incubated in a 50 μL system containing 5 mM $MgCl_2$, phosphatase inhibitor cocktail, and 50 mM

954 phosphate buffer (pH 7.1) at 30°C for 20 minutes. Following the pre-incubation, samples were
955 mixed with reaction buffer containing 20 mM HEPES (pH 7.1), 1 mM DTT, 1 mg/mL BSA, 4 mM
956 sodium citrate (pH 7.1), 5 mM $NaHCO_3$, 5 mM Mg-ATP (pH 7.1), 0.1 mM CoA, 1 mM NADPH,
957 and 0.025 µCi [1,5-^{14}C]citric acid (Revvity) in a total volume of 75 µL. The reactions were
958 incubated at 37°C for 15 minutes and terminated by adding 0.5 mL of cold methanol in 16 × 100
959 mm glass tubes (Corning). Next, 1.5 mL of methyl tert-butyl ether (MTBE) was added, and the
960 samples were vortexed thoroughly and left to stand at RT for 5 minutes. Then, 0.5 mL of ddH_2O
961 was added, followed by another round of vortexing and a 5-minute incubation at RT. Phase
962 separation was achieved by centrifugation at 2,000 × g for 5 minutes at RT. The upper organic
963 phase was transferred to scintillation vials and air-dried completely at RT. Dried lipids were
964 dissolved in 1 mL of methanol, and [^{14}C] radioactivity was quantified by liquid scintillation counting
965 (Beckman Coulter) after the addition of scintillation cocktail (Research Products International
966 Corp.).

967 **Phosphatase inhibitor cocktail preparation**

968 The phosphatase inhibitor cocktail was prepared fresh using the following recipe: sodium fluoride
969 (200 mM), imidazole (200 mM), sodium molybdate (115 mM), sodium orthovanadate (200 mM),
970 sodium tartrate dihydrate (400 mM), sodium pyrophosphate (100 mM), and β-glycerophosphate
971 (100 mM) in ddH_2O (final volume 20 mL). Sodium orthovanadate was prepared separately by
972 dissolving 1.84 g of powder in 50 mL ddH_2O, adjusting the pH to 10, briefly boiling in a microwave
973 (10 sec), cooling on ice to room temperature, and repeating the cycle three times. The solution
974 was adjusted to 50 mL, aliquoted, and stored at –20°C until use.

975 **Quantification and statistical analysis**

976 Sample sizes (n) are indicated in the figure legends. Technical replicates are also noted in the
977 figure legends when applicable. Unless otherwise stated, data are presented as mean ± SEM.
978 Statistical analyses were performed using GraphPad Prism 10. The statistical test and model
979 used for each experiment are specified in the corresponding figure legend. A significance
980 threshold of $\alpha = 0.05$ was used.
981 For co-localization analyses, images were quantified using Fiji/ImageJ (Coloc2). Pearson's
982 correlation coefficients were reported as values above the Costes threshold. Thresholded
983 Manders' coefficients (tM1 and tM2), Costes significance testing, and 2D intensity histograms
984 were generated using Coloc2 and are provided in the Supplemental Information.

985

986 ## Supplemental item titles

987 **Figure S1. Representative regions of interest (ROIs) and pixel-intensity scatter plots used**
988 **for colocalization analysis of ACC1, S14, and MIG12, related to Figure 1.**

989 **Figure S2. Sequential formation of the ACC1-containing lipogenic complex around LDs,**
990 **related to Figure 2.**

991 **Figure S3. Electron microscope images, related to Figure 3.**

992 **Figure S4. Phosphorylated ACC levels in liver lysates from rats refed the FFD, related to**
993 **Figure 4.**

994 **Figure S5. Physical association of ACC1 and ACC2 and regulation of TG synthesis by**
995 **phosphorylation in an $MgCl_2$-dependent manner, related to Figure 5.**

996 **Figure S6. Lipogenic metabolon formation facilitates FA production, related to Figure 6.**

997 **Figure S7. DAVID functional annotation of ACC1-dependent interactors from ACC1, MIG12,**
998 **and S14 immunoprecipitates, related to Figure 7.**

999 **Supplemental Table 1. Pearson's and Manders' colocalization coefficients together with**
1000 **Costes significance statistics for ACC1–MIG12, S14–MIG12, and S14–ACC1, related to**
1001 **Figure 1.**

1002 **Supplemental Table 2. Quantitative co-localization analysis of ACC1 with cytosolic**
1003 **lipogenic enzymes in primary hepatocytes, related to Figure 2.**

1004 **Supplemental Table 3. Original data of MS analysis of ACC1-dependent interactors from**
1005 **ACC1, MIG12, and S14 immunoprecipitates, related to Figure 7.**

1006

1007 ## References

1008 1. Sanders, F.W., and Griffin, J.L. (2016). De novo lipogenesis in the liver in health and disease:
1009 more than just a shunting yard for glucose. Biol Rev Camb Philos Soc *91*, 452-468.
1010 10.1111/brv.12178.
1011 2. Horton, J.D., Goldstein, J.L., and Brown, M.S. (2002). SREBPs:activators of the complete
1012 program of cholesterol and fatty acid synthesis in the liver. J. Clin. Invest. *109*, 1125-1131.
1013 3. Samuel, V.T., and Shulman, G.I. (2016). The pathogenesis of insulin resistance: integrating
1014 signaling pathways and substrate flux. J. Clin. Invest. *126*, 12-22. .

1015 4. Miao, T., Kim, J., Kang, P., Fujiwara, H., Hsu, F.F., and Bai, H. (2022). Acetyl-CoA-mediated
1016 autoacetylation of fatty acid synthase as a metabolic switch of de novo lipogenesis in
1017 Drosophila. Proc Natl Acad Sci U S A *119*, e2212220119. 10.1073/pnas.2212220119.
1018 5. Lin, H.P., Cheng, Z.L., He, R.Y., Song, L., Tian, M.X., Zhou, L.S., Groh, B.S., Liu, W.R., Ji, M.B.,
1019 Ding, C., et al. (2016). Destabilization of Fatty Acid Synthase by Acetylation Inhibits De Novo
1020 Lipogenesis and Tumor Cell Growth. Cancer Res *76*, 6924-6936. 10.1158/0008-5472.CAN-
1021 16-1597.
1022 6. Hellerstein, M.K. (1999). De novo lipogenesis in humans: metabolic and regulatory aspects.
1023 Eur. J. Clin. Nutr. *53*, S53-65.
1024 7. Parks, E.J., Krauss, R.M., Christiansen, M.P., Neese, R.A., and Hellerstein, M.K. (1999).
1025 Effects of a low-fat, high-carbohydrate diet on VLDL-triglyceride assembly, production, and
1026 clearance. J Clin Invest *104*, 1087-1096. 10.1172/JCI6572.
1027 8. Schwarz, J.M., Neese, R.A., Turner, S., Dare, D., and Hellerstein, M.K. (1995). Short-term
1028 alterations in carbohydrate energy intake in humans. Striking effects on hepatic glucose
1029 production, de novo lipogenesis, lipolysis, and whole-body fuel selection. J Clin Invest *96*,
1030 2735-2743. 10.1172/JCI118342.
1031 9. Donnelly, K.L., Smith, C.I., Schwarzenberg, S.J., Jessurun, J., Boldt, M.D., and Parks, E.J.
1032 (2005). Sources of fatty acids stored in liver and secreted via lipoproteins in patients with
1033 nonalcoholic fatty liver disease. J. Clin. Invest. *115*, 1343-1351.
1034 10. Ferre, P., and Foufelle, F. (2010). Hepatic steatosis: a role for de novo lipogenesis and the
1035 transcription factor SREBP-1c. Diabetes Obes Metab *12 Suppl 2*, 83-92. 10.1111/j.1463-
1036 1326.2010.01275.x.
1037 11. Lambert, J.E., Ramos-Roman, M.A., Browning, J.D., and Parks, E.J. (2014). Increased de novo
1038 lipogenesis is a distinct characteristic of individuals with nonalcoholic fatty liver disease.
1039 Gastroenterology *146*, 726-735. 10.1053/j.gastro.2013.11.049.
1040 12. Shimomura, I., Shimano, H., Korn, B.S., Bashmakov, Y., and Horton, J.D. (1998). Nuclear
1041 sterol regulatory element-binding proteins activate genes responsible for the entire program
1042 of unsaturated fatty acid biosynthesis in transgenic mouse liver. J. Biol. Chem. *273*, 35299-
1043 35306.
1044 13. Shimomura, I., Bashmakov, Y., and Horton, J.D. (1999). Increased levels of nuclear SREBP-
1045 1c associated with fatty livers in two mouse models of diabetes mellitus. J. Biol. Chem. *274*,
1046 30028-30032.
1047 14. Hudgins, L.C., Hellerstein, M., Seidman, C., Neese, R., Diakun, J., and Hirsch, J. (1996).
1048 Human fatty acid synthesis is stimulated by a eucaloric low fat, high carbohydrate diet. J Clin
1049 Invest *97*, 2081-2091. 10.1172/JCI118645.
1050 15. Eslam, M., Newsome, P.N., Sarin, S.K., Anstee, Q.M., Targher, G., Romero-Gomez, M.,
1051 Zelber-Sagi, S., Wai-Sun Wong, V., Dufour, J.F., Schattenberg, J.M., et al. (2020). A new
1052 definition for metabolic dysfunction-associated fatty liver disease: An international expert
1053 consensus statement. J Hepatol *73*, 202-209. 10.1016/j.jhep.2020.03.039.
1054 16. Cohen, J.C., Horton, J.D., and Hobbs, H.H. (2011). Human fatty liver disease: old questions
1055 and new insights. Science *332*, 1519-1523. 10.1126/science.1204265.
1056 17. Eslam, M., Sanyal, A.J., and George, J. (2020). MAFLD: A Consensus-Driven Proposed
1057 Nomenclature for Metabolic Associated Fatty Liver Disease. Gastroenterology *158*, 1999-
1058 2014.e1991. 10.1053/j.gastro.2019.11.312.
1059 18. Browning, J.D., Szczepaniak, L.S., Dobbins, R., Nuremberg, P., Horton, J.D., Cohen, J.C.,
1060 Grundy, S.M., and Hobbs, H.H. (2004). Prevalence of hepatic steatosis in an urban
1061 population in the United States: Impact of ethnicity. Hepatology *40*, 1387-1395.

1062 19. Shimano, H., Horton, J.D., Hammer, R.E., Shimomura, I., Brown, M.S., and Goldstein, J.L.
1063 (1996). Overproduction of cholesterol and fatty acids causes massive liver enlargement in
1064 transgenic mice expressing truncated SREBP-1a. J. Clin. Invest. *98*, 1575-1584.
1065 20. Horton, J.D., Bashmakov, Y., Shimomura, I., and Shimano, H. (1998). Regulation of sterol
1066 regulatory element binding proteins in livers of fasted and refed mice. Proc. Natl. Acad. Sci.
1067 U. S. A. *95*, 5987-5992.
1068 21. Horton, J.D., Shimomura, I., Brown, M.S., Hammer, R.E., Goldstein, J.L., and Shimano, H.
1069 (1998). Activation of cholesterol synthesis in preference to fatty acid synthesis in liver and
1070 adipose tissue of transgenic mice overproducing sterol regulatory element-binding protein-
1071 2. J. Clin. Invest. *101*, 2331-2339.
1072 22. Horton, J.D., Shimano, H., Hamilton, R.L., Brown, M.S., and Goldstein, J.L. (1999). Disruption
1073 of LDL receptor gene in transgenic SREBP-1a mice unmasks hyperlipidemia resulting from
1074 production of lipid-rich VLDL. J. Clin. Invest. *103*, 1067-1076.
1075 23. Matsuda, M., Korn, B.S., Hammer, R.E., Moon, Y.A., Komuro, R., Horton, J.D., Goldstein, J.L.,
1076 Brown, M.S., and Shimomura, I. (2001). SREBP cleavage-activating protein (SCAP) is required
1077 for increased lipid synthesis in liver induced by cholesterol deprivation and insulin elevation.
1078 Genes Dev. *15*, 1206-1216.
1079 24. Moon, Y.A., Liang, G., Xie, X., Frank-Kamenetsky, M., Fitzgerald, K., Koteliansky, V., Brown,
1080 M.S., Goldstein, J.L., and Horton, J.D. (2012). The Scap/SREBP pathway is essential for
1081 developing diabetic fatty liver and carbohydrate-induced hypertriglyceridemia in animals.
1082 Cell Metab. *15*, 240-246. 10.1016/j.cmet.2011.12.017.
1083 25. Abu-Elheiga, L., Brinkley, W.R., Zhong, L., Chirala, S.S., Woldegiorgis, G., and Wakil, S.J.
1084 (2000). The subcellular localization of acetyl-CoA carboxylase 2. Proc. Natl. Acad. Sci. U. S.
1085 A. *97*, 1444-1449.
1086 26. Man, W.C., Miyazaki, M., Chu, K., and Ntambi, J.M. (2006). Membrane topology of mouse
1087 stearoyl-CoA desaturase 1. J Biol Chem *281*, 1251-1260. 10.1074/jbc.M508733200.
1088 27. Moon, Y.-A., Shah, N.A., Mohapatra, S., Warrington, J.A., and Horton, J.D. (2001).
1089 Identification of a mammalian long chain fatty acyl elongase regulated by sterol regulatory
1090 element-binding proteins. J. Biol. Chem. *276*, 45358-45366.
1091 28. Gonzalez-Baró, M.R., Granger, D.A., and Coleman, R.A. (2001). Mitochondrial Glycerol
1092 Phosphate Acyltransferase Contains Two Transmembrane Domains with the Active Site in
1093 the N-terminal Domain Facing the Cytosol. Journal of Biological Chemistry *276*, 43182-
1094 43188. 10.1074/jbc.M107885200.
1095 29. P.A., S. (1972). Is there an organization of Krebs cycle enzymes in the mitochondrial matrix?
1096 In: Mehlman M.A., Hanson R.W., editors. Energy Metabolism and the Regulation of Metabolic
1097 Processes in Mitochondria. Academic Press; New York, pp. 79–91.
1098 30. P.A., S. (1985). The metabolon. Trends Biochem. Sci., 10:109–110.
1099 31. Bulutoglu, B., Garcia, K.E., Wu, F., Minteer, S.D., and Banta, S. (2016). Direct Evidence for
1100 Metabolon Formation and Substrate Channeling in Recombinant TCA Cycle Enzymes. ACS
1101 Chem Biol *11*, 2847-2853. 10.1021/acschembio.6b00523.
1102 32. Robinson, J.B., Jr., Inman, L., Sumegi, B., and Srere, P.A. (1987). Further characterization of
1103 the Krebs tricarboxylic acid cycle metabolon. J Biol Chem *262*, 1786-1790.
1104 33. Kohnhorst, C.L., Kyoung, M., Jeon, M., Schmitt, D.L., Kennedy, E.L., Ramirez, J., Bracey, S.M.,
1105 Luu, B.T., Russell, S.J., and An, S. (2017). Identification of a multienzyme complex for glucose
1106 metabolism in living cells. J Biol Chem *292*, 9191-9203. 10.1074/jbc.M117.783050.
1107 34. Colbert, C.L., Kim, C.W., Moon, Y.A., Henry, L., Palnitkar, M., McKean, W.B., Fitzgerald, K.,
1108 Deisenhofer, J., Horton, J.D., and Kwon, H.J. (2010). Crystal structure of Spot 14, a modulator
1109 of fatty acid synthesis. Proc Natl Acad Sci U S A *107*, 18820-18825. 1012736107 [pii]

1110 10.1073/pnas.1012736107.
1111 35. Jump, D.B., and Oppenheimer, J.H. (1985). High basal expression and 3,5,3'-triiodothyronine
1112 regulation of messenger ribonucleic acid S14 in lipogenic tissues. Endocrinology *117*, 2259-
1113 2266. 10.1210/endo-117-6-2259.
1114 36. Horton, J.D., Shah, N.A., Warrington, J.A., Anderson, N.N., Park, S.W., Brown, M.S., and
1115 Goldstein, J.L. (2003). Combined analysis of oligonucleotide microarray data from
1116 transgenic and knockout mice identifies direct SREBP target genes. Proc. Natl. Acad. Sci. U.
1117 S. A. *100*, 12027-12032.
1118 37. Mater, M.K., Thelen, A.P., Pan, D.A., and Jump, D.B. (1999). Sterol response element-binding
1119 protein 1c (SREBP1c) is involved in the polyunsaturated fatty acid suppression of hepatic S14
1120 gene transcription. J. Biol. Chem. *274*, 32725-32732.
1121 38. Ma, L., Tsatsos, N.G., and Towle, H.C. (2005). Direct role of ChREBP·Mlx in regulating hepatic
1122 glucose-responsive genes. J. Biol. Chem. *280*, 12019-12027. 10.1074/jbc.M413063200.
1123 39. Seelig, S., Liaw, C., Towle, H.C., and Oppenheimer, J.H. (1981). Thyroid hormone attenuates
1124 and augments hepatic gene expression at a pretranslational level. Proc. Natl. Acad. Sci. U.
1125 S. A. *78*, 4733-4737.
1126 40. Zhu, Q., Anderson, G.W., Mucha, G.T., Parks, E.J., Metkowski, J.K., and Mariash, C.N. (2005).
1127 The Spot 14 protein is required for de novo lipid synthesis in the lactating mammary gland.
1128 Endocrinology *146*, 3343-3350.
1129 41. Kim, C.W., Moon, Y.A., Park, S.W., Cheng, D., Kwon, H.J., and Horton, J.D. (2010). Induced
1130 polymerization of mammalian acetyl-CoA carboxylase by MIG12 provides a tertiary level of
1131 regulation of fatty acid synthesis. Proc. Natl. Acad. Sci. U. S. A. *107*, 9626-9631.
1132 42. Ha, J., Daniel, S., Broyles, S.S., and Kim, K.H. (1994). Critical phosphorylation sites for acetyl-
1133 CoA carboxylase activity. J Biol Chem *269*, 22162-22168.
1134 43. Locke, G.A., Cheng, D., Witmer, M.R., Tamura, J.K., Haque, T., Carney, R.F., Rendina, A.R.,
1135 and Marcinkeviciene, J. (2008). Differential activation of recombinant human acetyl-CoA
1136 carboxylases 1 and 2 by citrate. Arch. Biochem. Biophys. *475*, 72-79. S0003-9861(08)00196-
1137 3 [pii]

1138 10.1016/j.abb.2008.04.011 [doi].
1139 44. Kahn, B.B., Alquier, T., Carling, D., and Hardie, D.G. (2005). AMP-activated protein kinase:
1140 Ancient energy gauge provides clues to modern understanding of metabolism. Cell
1141 Metabolism *1*, 15-25. DOI: 10.1016/j.cmet.2004.12.003.
1142 45. Witters, L.A., Watts, T.D., Daniels, D.L., and Evans, J.L. (1988). Insulin stimulates the
1143 dephosphorylation and activation of acetyl-CoA carboxylase. Proc. Natl. Acad. Sci. U. S. A.
1144 *85*, 5473-5477.
1145 46. Berglund, E.D., Lustig, D.G., Baheza, R.A., Hasenour, C.M., Lee-Young, R.S., Donahue, E.P.,
1146 Lynes, S.E., Swift, L.L., Charron, M.J., Damon, B.M., and Wasserman, D.H. (2011). Hepatic
1147 glucagon action is essential for exercise-induced reversal of mouse fatty liver. Diabetes *60*,
1148 2720-2729. 10.2337/db11-0455.
1149 47. Munday, M.R., Milic, M.R., Takhar, S., Holness, M.J., and Sugden, M.C. (1991). The short-term
1150 regulation of hepatic acetyl-CoA carboxylase during starvation and re-feeding in the rat.
1151 Biochem J *280 (Pt 3)*, 733-737. 10.1042/bj2800733.
1152 48. Berglund, E.D., Lee-Young, R.S., Lustig, D.G., Lynes, S.E., Donahue, E.P., Camacho, R.C.,
1153 Meredith, M.E., Magnuson, M.A., Charron, M.J., and Wasserman, D.H. (2009). Hepatic energy
1154 state is regulated by glucagon receptor signaling in mice. J Clin Invest *119*, 2412-2422.
1155 10.1172/jci38650.

1156 49. Kimball, S.R., Siegfried, B.A., and Jefferson, L.S. (2004). Glucagon represses signaling
1157 through the mammalian target of rapamycin in rat liver by activating AMP-activated protein
1158 kinase. J Biol Chem *279*, 54103-54109. 10.1074/jbc.M410755200.
1159 50. Ragolia, L., and Begum, N. (1998). Protein phosphatase-1 and insulin action. Mol Cell
1160 Biochem *182*, 49-58.
1161 51. Kim, K.H. (1983). Regulation of acetyl-CoA carboxylase. Curr Top Cell Regul *22*, 143-176.
1162 10.1016/b978-0-12-152822-5.50009-9.
1163 52. Kim, K.H., Lopez-Casillas, F., Bai, D.H., Luo, X., and Pape, M.E. (1989). Role of reversible
1164 phosphorylation of acetyl-CoA carboxylase in long-chain fatty acid synthesis. FASEB J *3*,
1165 2250-2256. 10.1096/fasebj.3.11.2570725.
1166 53. Fediuc, S., Gaidhu, M.P., and Ceddia, R.B. (2006). Regulation of AMP-activated protein
1167 kinase and acetyl-CoA carboxylase phosphorylation by palmitate in skeletal muscle cells. J
1168 Lipid Res *47*, 412-420. 10.1194/jlr.M500438-JLR200.
1169 54. Wang, Y., Viscarra, J., Kim, S.-J., and Sul, H.S. (2015). Transcriptional regulation of hepatic
1170 lipogenesis. Nature reviews. Molecular cell biology *16*, 678-689. 10.1038/nrm4074.
1171 55. Umlauf, E., Csaszar, E., Moertelmaier, M., Schuetz, G.J., Parton, R.G., and Prohaska, R.
1172 (2004). Association of stomatin with lipid bodies. J Biol Chem *279*, 23699-23709.
1173 10.1074/jbc.M310546200.
1174 56. Liu, P., Ying, Y., Zhao, Y., Mundy, D.I., Zhu, M., and Anderson, R.G. (2004). Chinese hamster
1175 ovary K2 cell lipid droplets appear to be metabolic organelles involved in membrane traffic.
1176 J Biol Chem *279*, 3787-3792. 10.1074/jbc.M311945200.
1177 57. Bartz, R., Zehmer, J.K., Zhu, M., Chen, Y., Serrero, G., Zhao, Y., and Liu, P. (2007). Dynamic
1178 activity of lipid droplets: protein phosphorylation and GTP-mediated protein translocation. J
1179 Proteome Res *6*, 3256-3265. 10.1021/pr070158j.
1180 58. Beller, M., Riedel, D., Jansch, L., Dieterich, G., Wehland, J., Jackle, H., and Kuhnlein, R.P.
1181 (2006). Characterization of the Drosophila lipid droplet subproteome. Molecular & cellular
1182 proteomics : MCP *5*, 1082-1094. 10.1074/mcp.M600011-MCP200.
1183 59. Wan, H.C., Melo, R.C., Jin, Z., Dvorak, A.M., and Weller, P.F. (2007). Roles and origins of
1184 leukocyte lipid bodies: proteomic and ultrastructural studies. FASEB J *21*, 167-178.
1185 10.1096/fj.06-6711com.
1186 60. Lyubarev, A.E., and Kurganov, B.I. (1989). Supramolecular organization of tricarboxylic acid
1187 cycle enzymes. Biosystems *22*, 91-102. 10.1016/0303-2647(89)90038-5.
1188 61. Kurganov B. I, L.A.E. (1988). Hypothetical structure of the complex of glycolytic enzymes
1189 (glycolytic metabolon), formed on the membrane of erythrocytes. Molek. Biologia. *V.22,*
1190 *No.6*, p. 1605–1613.
1191 62. Graham, J.W., Williams, T.C., Morgan, M., Fernie, A.R., Ratcliffe, R.G., and Sweetlove, L.J.
1192 (2007). Glycolytic enzymes associate dynamically with mitochondria in response to
1193 respiratory demand and support substrate channeling. Plant Cell *19*, 3723-3738.
1194 10.1105/tpc.107.053371.
1195 63. Srere, P.A. (1974). Controls of citrate synthase activity. Life Sci *15*, 1695-1710.
1196 10.1016/0024-3205(74)90172-6.
1197 64. Webb, B.A., Dosey, A.M., Wittmann, T., Kollman, J.M., and Barber, D.L. (2017). The glycolytic
1198 enzyme phosphofructokinase-1 assembles into filaments. J Cell Biol *216*, 2305-2313.
1199 10.1083/jcb.201701084.
1200 65. Kastritis, P.L., O'Reilly, F.J., Bock, T., Li, Y., Rogon, M.Z., Buczak, K., Romanov, N., Betts, M.J.,
1201 Bui, K.H., Hagen, W.J., et al. (2017). Capturing protein communities by structural proteomics
1202 in a thermophilic eukaryote. Mol Syst Biol *13*, 936. 10.15252/msb.20167412.

1203 66. Suresh, H.G., da Silveira Dos Santos, A.X., Kukulski, W., Tyedmers, J., Riezman, H., Bukau,
1204 B., and Mogk, A. (2015). Prolonged starvation drives reversible sequestration of lipid
1205 biosynthetic enzymes and organelle reorganization in Saccharomyces cerevisiae. Mol Biol
1206 Cell *26*, 1601-1615. 10.1091/mbc.E14-11-1559.
1207 67. Wijesinghe, K.M., Kim, C.W., Schad, E.O., Li, S., Chen, S., Takeshima, E., Khandwala, C.B.,
1208 Tillo, D., Lebensohn, A.M., Olzmann, J.A., et al. (2025). Plasma membrane accessible
1209 cholesterol is regulated by ACC1 and lipid droplets. bioRxiv. 10.1101/2025.08.21.671640.
1210 68. Zhou, F., Zhang, Y., Zhu, Y., Zhou, Q., Shi, Y., and Hu, Q. (2024). Filament structures unveil
1211 the dynamic organization of human acetyl-CoA carboxylase. Sci Adv *10*, eado4880.
1212 10.1126/sciadv.ado4880.
1213 69. Hunkeler, M., Hagmann, A., Stuttfeld, E., Chami, M., Guri, Y., Stahlberg, H., and Maier, T.
1214 (2018). Structural basis for regulation of human acetyl-CoA carboxylase. Nature *558*, 470-
1215 474. 10.1038/s41586-018-0201-4.
1216 70. Møller, B.L. (2010). Plant science. Dynamic metabolons. Science *330*, 1328-1329.
1217 10.1126/science.1194971.
1218 71. Kim, C.W., Addy, C., Kusunoki, J., Anderson, N.N., Deja, S., Fu, X., Burgess, S.C., Li, C.,
1219 Ruddy, M., Chakravarthy, M., et al. (2017). Acetyl CoA Carboxylase Inhibition Reduces
1220 Hepatic Steatosis but Elevates Plasma Triglycerides in Mice and Humans: A Bedside to
1221 Bench Investigation. Cell Metab *26*, 394-406. e396. 10.1016/j.cmet.2017.07.009.
1222 72. Kim, C.W., Moon, Y.A., Park, S.W., Cheng, D., Kwon, H.J., and Horton, J.D. (2010). Induced
1223 polymerization of mammalian acetyl-CoA carboxylase by MIG12 provides a tertiary level of
1224 regulation of fatty acid synthesis. Proc Natl Acad Sci U S A *107*, 9626-9631.
1225 10.1073/pnas.1001292107.
1226 73. Shimomura, I., Hammer, R.E., Ikemoto, S., Brown, M.S., and Goldstein, J.L. (1999). Leptin
1227 reverses insulin resistance and diabetes mellitus in mice with congenital lipodystrophy.
1228 Nature *401*, 73-76.
1229 74. Lagace, T.A., Curtis, D.E., Garuti, R., McNutt, M.C., Park, S.W., Prather, H.B., Anderson, N.N.,
1230 Ho, Y.K., Hammer, R.E., and Horton, J.D. (2006). Secreted PCSK9 decreases the number of
1231 LDL receptors in hepatocytes and in livers of parabiotic mice. J Clin Invest *116*, 2995-3005.
1232 10.1172/jci29383.
1233 75. Herz, J., Kowal, R.C., Ho, Y.K., Brown, M.S., and Goldstein, J.L. (1990). Low density
1234 lipoprotein receptor-related protein mediates endocytosis of monoclonal antibodies in
1235 cultured cells and rabbit liver. J Biol Chem *265*, 21355-21362.
1236 76. Engelking, L.J., Kuriyama, H., Hammer, R.E., Horton, J.D., Brown, M.S., Goldstein, J.L., and
1237 Liang, G. (2004). Overexpression of Insig-1 in the livers of transgenic mice inhibits SREBP
1238 processing and reduces insulin-stimulated lipogenesis. J. Clin. Invest. *113*, 1168-1175.
1239 77. Yamamoto, A., and Masaki, R. (2010). Pre-embedding nanogold silver and gold
1240 intensification. Methods Mol Biol *657*, 225-235. 10.1007/978-1-60761-783-9_18.
1241 78. Ding, Y., Zhang, S., Yang, L., Na, H., Zhang, P., Zhang, H., Wang, Y., Chen, Y., Yu, J., Huo, C.,
1242 et al. (2013). Isolating lipid droplets from multiple species. Nat Protoc *8*, 43-51.
1243 10.1038/nprot.2012.142.

1244

1245

Figure 1

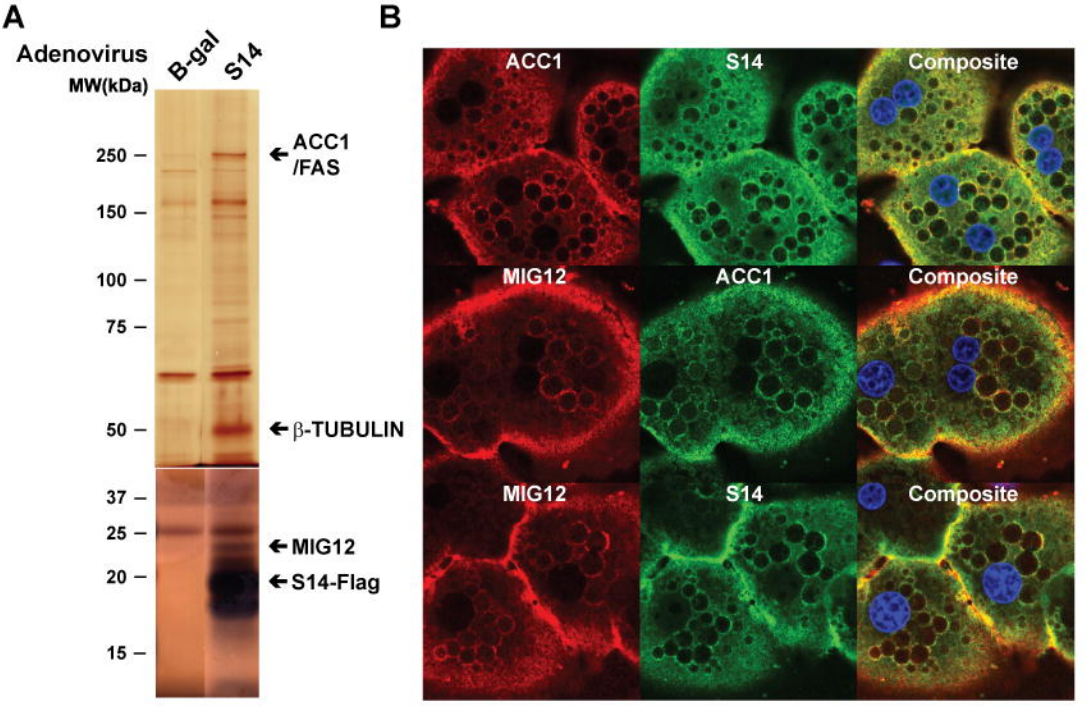
A
Adenovirus
B-gal
S14
MW(kDa)
250
150
100
75
50
37
25
20
15
ACC1
/FAS
β-TUBULIN
MIG12
S14-Flag
B
ACC1
S14
Composite
MIG12
ACC1
Composite
MIG12
S14
Composite

Figure 2

A

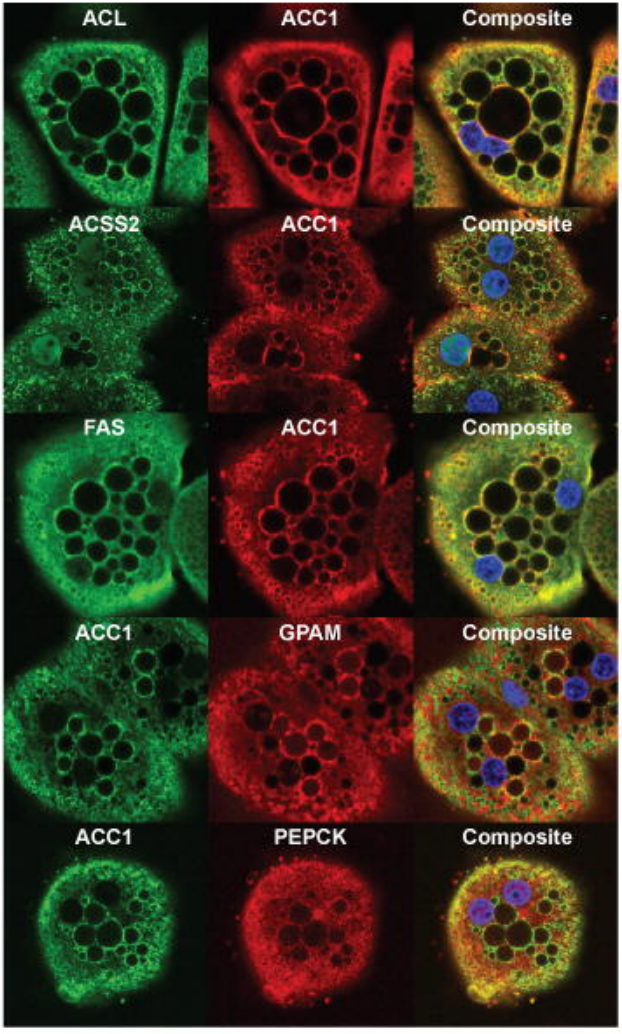
ACL
ACC1
Composite
ACSS2
ACC1
Composite
FAS
ACC1
Composite
ACC1
GPAM
Composite
ACC1
PEPCK
Composite

B

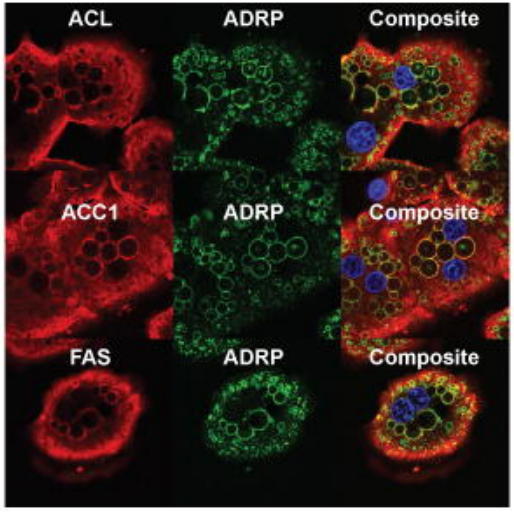
ACL
ADRP
Composite
ACC1
ADRP
Composite
FAS
ADRP
Composite

C

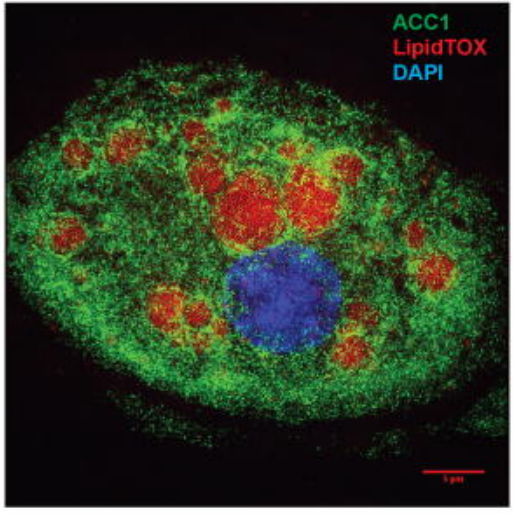
ACC1
LipidTOX
DAPI

Figure 3

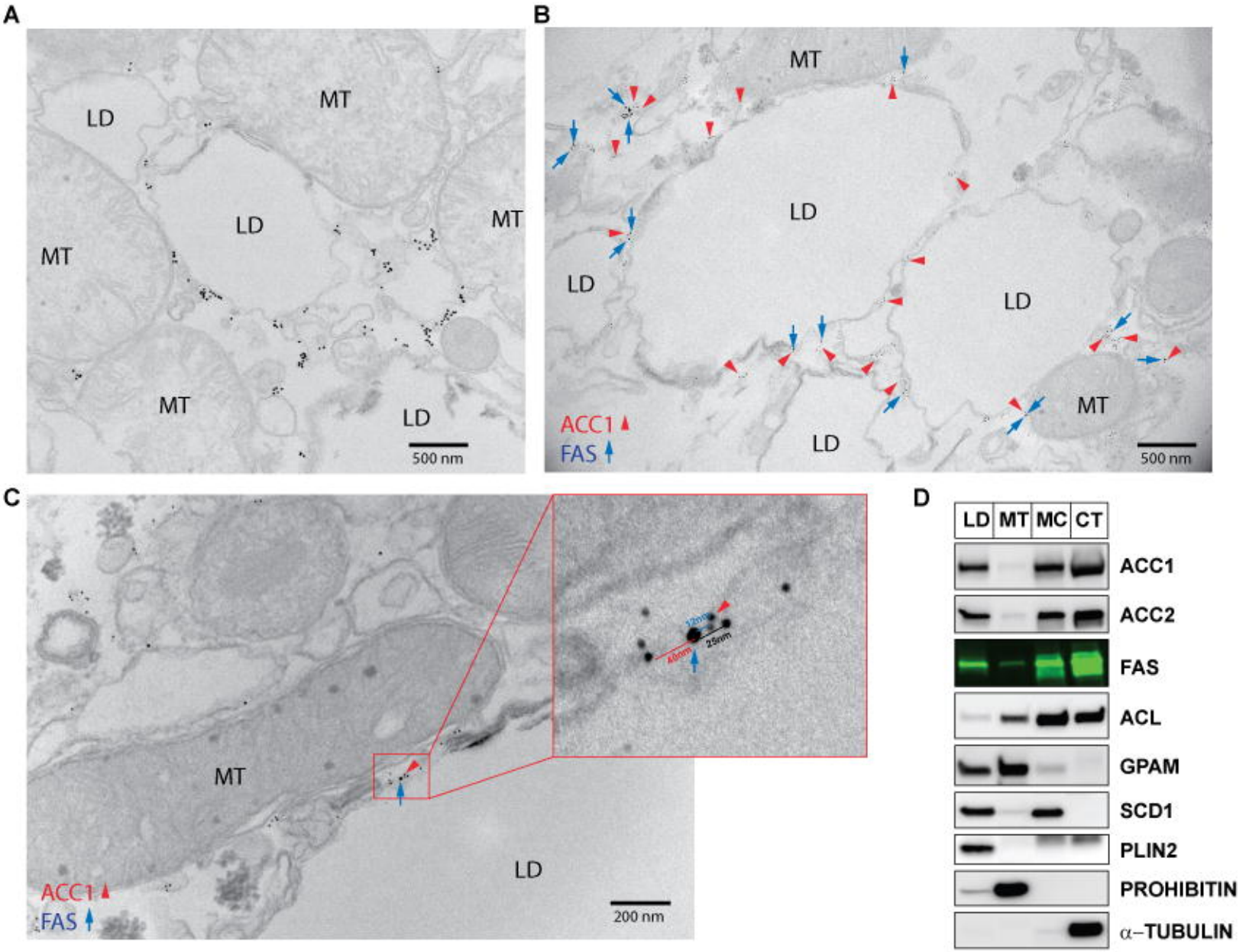
A
LD
MT
LD
MT
MT
MT
LD
500 nm
B
MT
LD
LD
LD
MT
LD
ACC1
FAS
500 nm
C
MT
LD
ACC1
FAS
200 nm
D
LD
MT
MC
CT
ACC1
ACC2
FAS
ACL
GPAM
SCD1
PLIN2
PROHIBITIN
α–TUBULIN

Figure 4

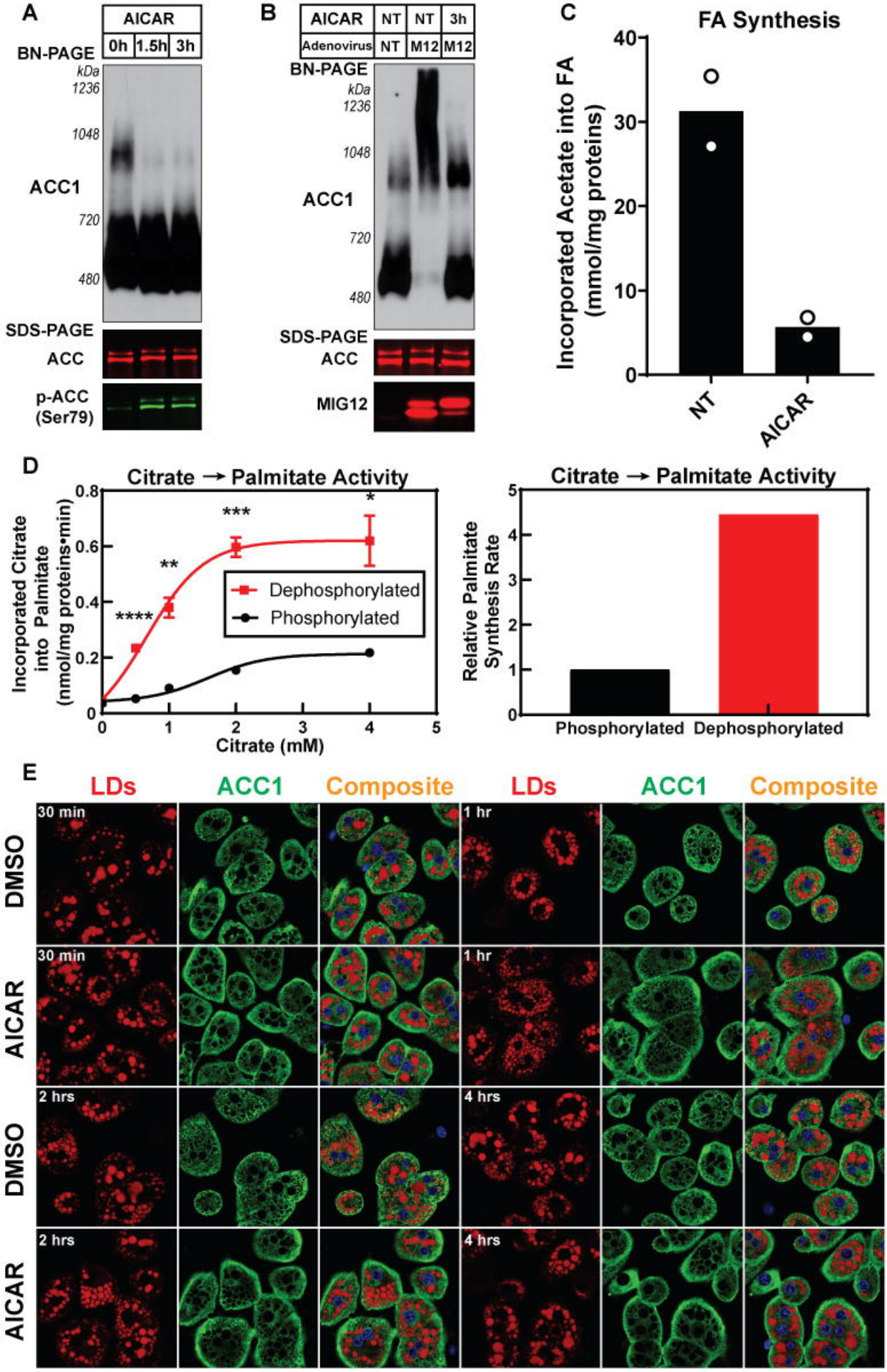
A
AICAR
0h
1.5h
3h
BN-PAGE
kDa
1236
1048
ACC1
720
480
SDS-PAGE
ACC
p-ACC
(Ser79)
B
AICAR
NT
NT
3h
Adenovirus
NT
M12
M12
BN-PAGE
kDa
1236
1048
ACC1
720
480
SDS-PAGE
ACC
MIG12
C
FA Synthesis
Incorporated Acetate into FA
(mmol/mg proteins)
40
30
20
10
0
NT
AICAR
D
Citrate → Palmitate Activity
Incorporated Citrate
into Palmitate
(nmol/mg proteins•min)
0.8
0.6
0.4
0.2
0
****
**
***
*
Dephosphorylated
Phosphorylated
0
1
2
3
4
5
Citrate (mM)
Citrate → Palmitate Activity
Relative Palmitate
Synthesis Rate
5
4
3
2
1
0
Phosphorylated
Dephosphorylated
E
LDs
ACC1
Composite
LDs
ACC1
Composite
DMSO
AICAR
DMSO
AICAR
30 min
1 hr
30 min
1 hr
2 hrs
4 hrs
2 hrs
4 hrs

Figure 5

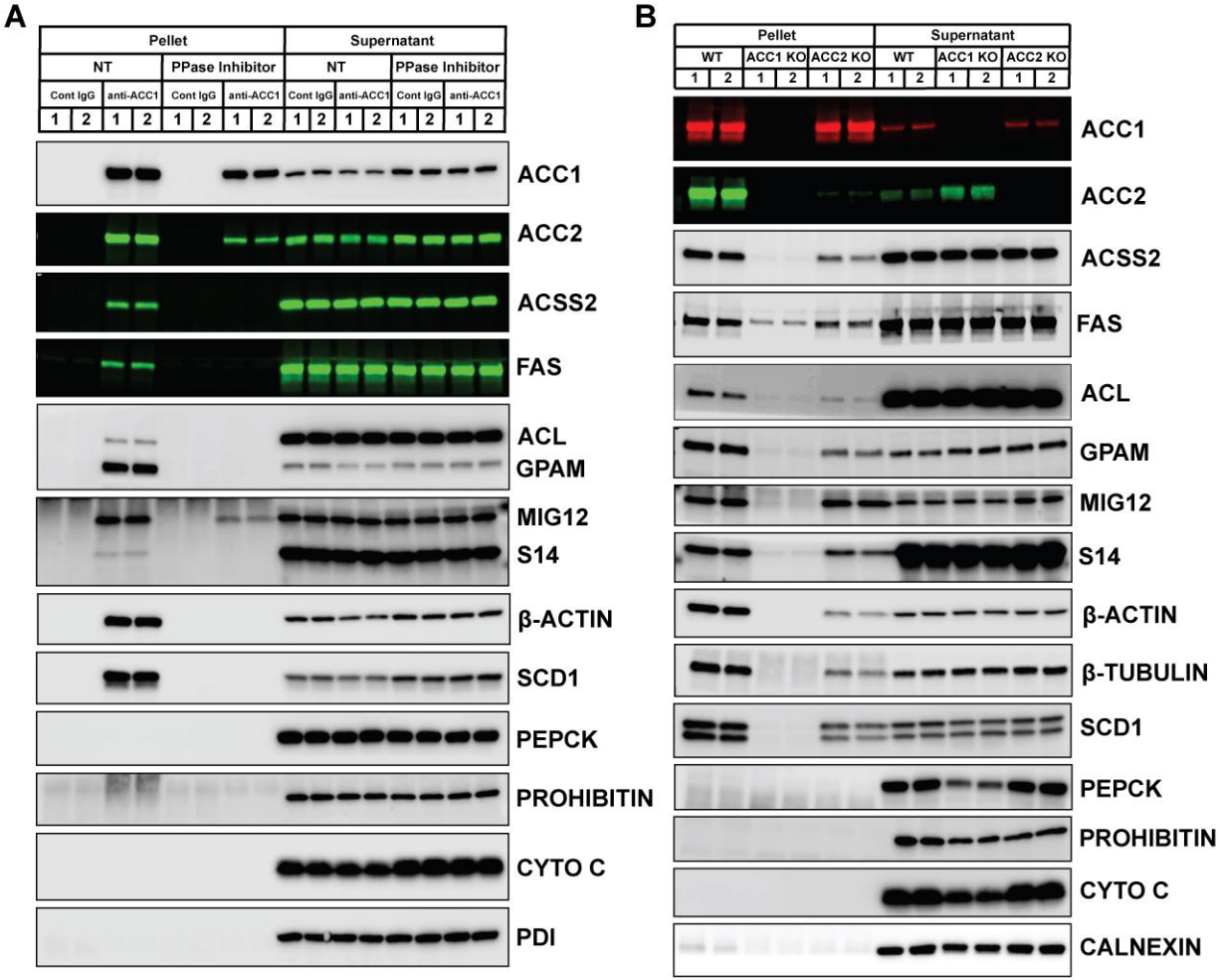
A
Pellet
Supernatant
NT
PPase Inhibitor
NT
PPase Inhibitor
Cont IgG
anti-ACC1
Cont IgG
anti-ACC1
Cont IgG
anti-ACC1
Cont IgG
anti-ACC1
1 2 1 2 1 2 1 2 1 2 1 2 1 2 1 2
ACC1
ACC2
ACSS2
FAS
ACL
GPAM
MIG12
S14
β-ACTIN
SCD1
PEPCK
PROHIBITIN
CYTO C
PDI
B
Pellet
Supernatant
WT
ACC1 KO
ACC2 KO
WT
ACC1 KO
ACC2 KO
1 2 1 2 1 2 1 2 1 2 1 2
ACC1
ACC2
ACSS2
FAS
ACL
GPAM
MIG12
S14
β-ACTIN
β-TUBULIN
SCD1
PEPCK
PROHIBITIN
CYTO C
CALNEXIN

Figure 6

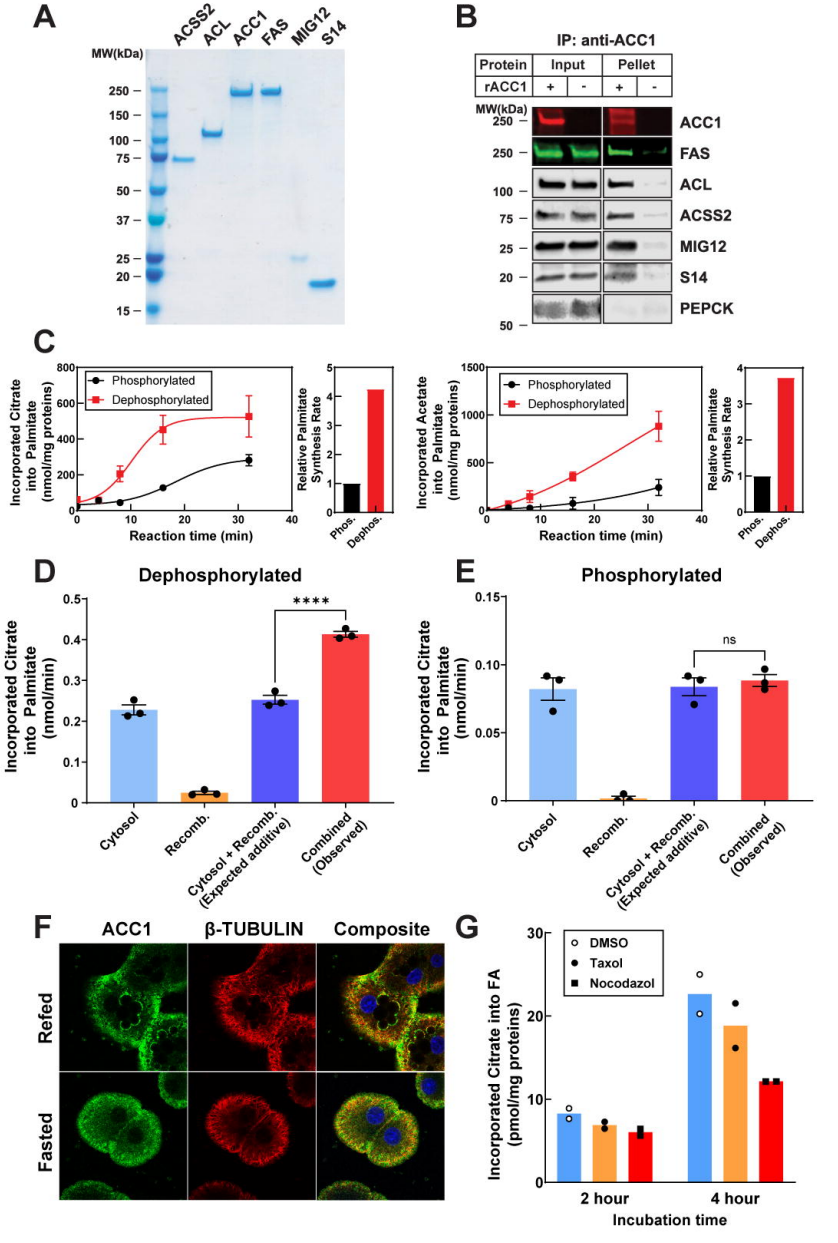
A
ACSS2
ACL
ACC1
FAS
MIG12
S14
MW(kDa)
250
150
100
75
50
37
25
20
15
B
IP: anti-ACC1
Protein
Input
Pellet
rACC1
+
-
+
-
MW(kDa)
ACC1
FAS
ACL
ACSS2
MIG12
S14
PEPCK
C
Phosphorylated
Dephosphorylated
Incorporated Citrate into Palmitate (nmol/mg proteins)
Reaction time (min)
Relative Palmitate Synthesis Rate
Phos.
Dephos.
Incorporated Acetate into Palmitate (nmol/mg proteins)
D
Dephosphorylated
Incorporated Citrate into Palmitate (nmol/min)
****
Cytosol
Recomb.
Cytosol + Recomb. (Expected additive)
Combined (Observed)
E
Phosphorylated
ns
F
ACC1
β-TUBULIN
Composite
Refed
Fasted
G
DMSO
Taxol
Nocodazol
Incorporated Citrate into FA (pmol/mg proteins)
2 hour
4 hour
Incubation time

Figure 7

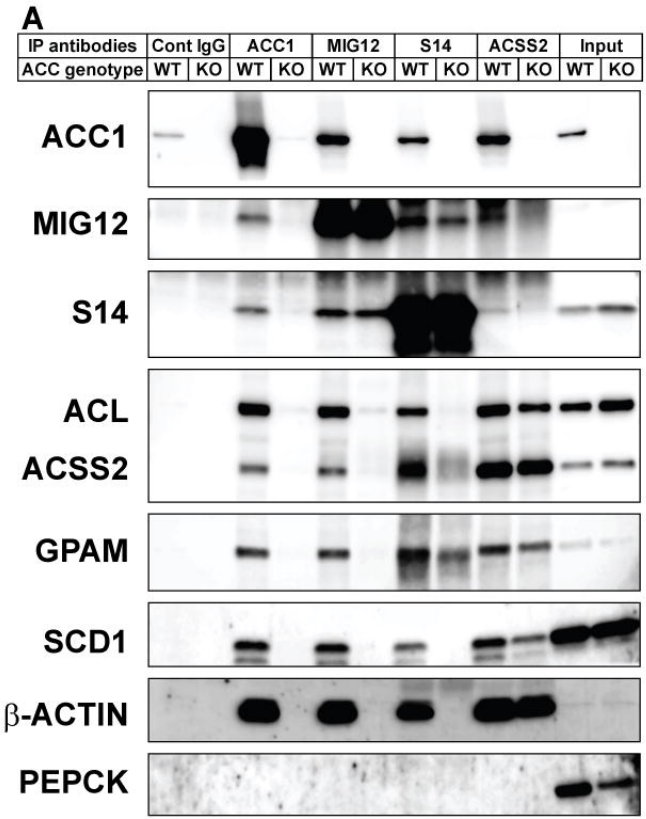
A
IP antibodies
Cont IgG
ACC1
MIG12
S14
ACSS2
Input
ACC genotype
WT
KO
ACC1
MIG12
S14
ACL
ACSS2
GPAM
SCD1
β-ACTIN
PEPCK

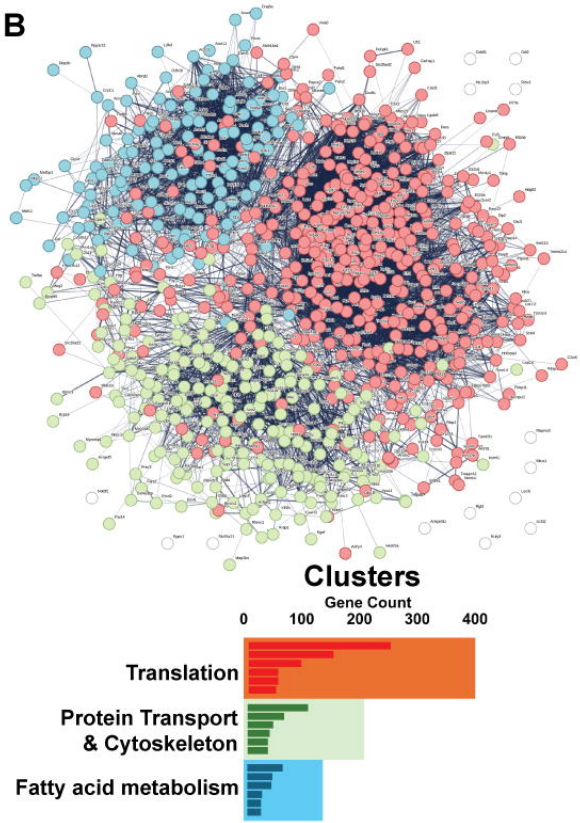
B
Clusters
Gene Count
0
100
200
300
400
Translation
Protein Transport
& Cytoskeleton
Fatty acid metabolism